Cell Reports
Medicine

Article

AdipoAtlas: A reference lipidome for human white adipose tissue

Graphical abstract

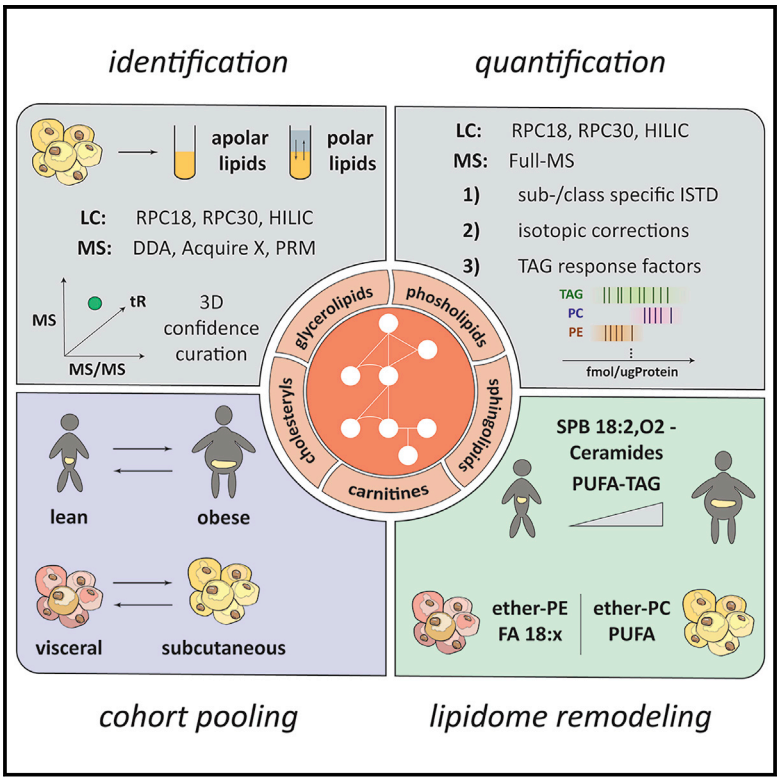

Highlights

- *AdipoAtlas* provides a reference lipidome of human white adipose tissue
- 1,636 and 737 lipids were identified and quantified by tissue tailored LC-MS lipidomics
- *AdipoAtlas* demonstrates prominent differences between subcutaneous and visceral tissue depots
- Obesity leads to the remodeling of sphingo-, ether-, and neutral lipid metabolism

Authors

Mike Lange, Georgia Angelidou, Zhixu Ni, Angela Criscuolo, Jürgen Schiller, Matthias Blüher, Maria Fedorova

Correspondence

maria.fedorova@tu-dresden.de

In brief

Lange et al. report a reference lipidome of human white adipose tissue by providing qualitative and quantitative analyses of lipid compositions in lean and obese states for subcutaneous and visceral depots. Several key events of lipidome remodeling in obesity are identified within the metabolism of sphingo-, ether-, and neutral lipids.

Lange et al., 2021, Cell Reports Medicine *2*, 100407
October 19, 2021
https://doi.org/10.1016/j.xcrm.2021.100407

CellPress

Cell Reports Medicine

CellPress
OPEN ACCESS

Article

AdipoAtlas: A reference lipidome for human white adipose tissue

Mike Lange,[1,2,7] Georgia Angelidou,[1,2] Zhixu Ni,[1,2,8] Angela Criscuolo,[1,2,3] Jürgen Schiller,[4] Matthias Blüher,[5,6] and Maria Fedorova[1,2,8,9,*]

[1]Institute of Bioanalytical Chemistry, Faculty of Chemistry and Mineralogy, University of Leipzig, Leipzig, Germany
[2]Center for Biotechnology and Biomedicine, University of Leipzig, Leipzig, Germany
[3]Thermo Fisher Scientific, Dreieich, Germany
[4]Institute of Medical Physics and Biophysics, Medical Faculty, University of Leipzig, Leipzig, Germany
[5]Medical Department III (Endocrinology, Nephrology and Rheumatology), University of Leipzig, Leipzig, Germany
[6]Helmholtz Institute for Metabolic, Obesity and Vascular Research (HI-MAG) of the Helmholtz Zentrum München at the University of Leipzig and University Hospital Leipzig, Leipzig, Germany
[7]Present address: Department of Nutritional Sciences & Toxicology and Molecular and Cell Biology, University of California, Berkeley, CA, USA
[8]Present address: Center of Membrane Biochemistry and Lipid Research, Department of Membrane Biochemistry and Lipid Metabolism, University Hospital and Faculty of Medicine Carl Gustav Carus of TU Dresden, Dresden, Germany
[9]Lead contact
*Correspondence: maria.fedorova@tu-dresden.de
https://doi.org/10.1016/j.xcrm.2021.100407

SUMMARY

Obesity, characterized by expansion and metabolic dysregulation of white adipose tissue (WAT), has reached pandemic proportions and acts as a primer for a wide range of metabolic disorders. Remodeling of WAT lipidome in obesity and associated comorbidities can explain disease etiology and provide valuable diagnostic and prognostic markers. To support understanding of WAT lipidome remodeling at the molecular level, we provide in-depth lipidomics profiling of human subcutaneous and visceral WAT of lean and obese individuals. We generate a human WAT reference lipidome by performing tissue-tailored preanalytical and analytical workflows, which allow accurate identification and semi-absolute quantification of 1,636 and 737 lipid molecular species, respectively. Deep lipidomic profiling allows identification of main lipid (sub)classes undergoing depot-/phenotype-specific remodeling. Previously unanticipated diversity of WAT ceramides is now uncovered. *AdipoAtlas* reference lipidome serves as a data-rich resource for the development of WAT-specific high-throughput methods and as a scaffold for systems medicine data integration.

INTRODUCTION

The "industrial revolution" in modern omics technologies significantly enriched our understanding of human biology. Application of high-throughput transcriptomics and proteomics allowed to compile the Tissue Atlas within the Human Proteome Atlas project with expression levels of mRNA and proteins reported for 44 healthy human tissues, serving as a powerful resource for exploration of functional tissue specificities, future drug targets, and potential biomarkers.[1] Lipidomics, an omics branch aiming to identify and quantify individual lipid species, is not yet as advanced in the characterization of cell-, tissue-, and organ-specific lipid compositions. The majority of lipidomics studies aim for high-throughput screening of large sample cohorts and clinical translation.[2,3] Such analytical workflows, targeting robust applications, are optimized for bulk lipid extraction followed by a single analysis method and relative (disease versus control) quantification.

Considering the cooperative action of lipids in biological membranes and the tight coregulation of anabolic and catabolic pathways of lipid metabolism, identification of tissue- and cell-type-specific lipid signatures (reference lipidomes) is urgently required to facilitate deeper understanding of lipid biology in health and disease. Lipid cooperative actions are highly tissue/cell-type specific at all levels of their functional activities, including plasticity of cellular membranes, energy storage, redistribution, and coordinated signaling.[4,5] Furthermore, capturing alterations in lipid metabolism might be as important as identifying static lipid signatures resistant to certain (patho)physiological stimuli.

Deep lipidome profiling cannot be performed in a high-throughput manner, as it requires tissue-specific optimization and application of several orthogonal analytical methods to ensure simultaneous coverage of lipid classes with different polarities, ionization properties, and a range of endogenous concentrations. By now, the best-characterized composition is available for the blood plasma lipidome, with around 600 lipid species described at lipid class and lipid molecular species levels.[6–8] However, detailed quantitative inventory of peripheral tissue lipidomes is scarce. Currently, adipose tissue metabolism

is attracting a lot of scientific attention. Obesity, characterized by white adipose tissue (WAT) expansion and metabolic dysregulation, has reached pandemic proportions in modern societies, with a prevalence of more than 20% of the population.[9] Obesity is associated with an increased threat of premature death due to a significantly higher risk of developing type 2 diabetes mellitus (T2DM), hypertension, coronary heart disease, stroke, and several types of cancer. Remodeling of WAT metabolism in obesity and, importantly, in the development of metabolic complications, is a cornerstone in understanding disease etiology. So far, WAT metabolism has been studied from many different angles, including genetic predisposition to obesity via genome-wide association studies[10] and changes in transcriptomics,[11] epigenetic,[12] and proteomics[13] patterns of WAT upon obesity development. However, studies reporting the detailed quantitative description of depot-specific (subcutaneous [SAT] versus visceral [VAT]) WAT lipidomes in lean and obese human individuals are limited.

Here, we present *AdipoAtlas*: a mass-spectrometry-based reference lipidome of human WAT reporting over 1600 and 700 lipid species on qualitative and quantitative levels, respectively. *AdipoAtlas* represents a data-rich resource freely available to all lipid researchers, will support further understanding of lipidomic alterations within human adipose tissue, and acts as a guideline to generate other tissue-specific lipidome maps.

RESULTS

WAT-tailored lipid extraction and fractionation

WAT acts as the main lipid storage organ, with triacylglycerol (TG) present at exceedingly high concentrations, masking other less abundant lipid classes (Figure 1A). For accurate molecular mapping of the WAT lipidome, both extraction and fractionation were optimized to ensure coverage of both highly abundant storage (TG) and less abundant membrane and signaling (phospholipids [PLs] and sphingolipids [SPs]) lipids. To support in-depth lipidome profiling, we created tissue pools of WAT representing SAT and VAT depots of lean (n = 5; BMI = 23.1 ± 1.5 kg/m^2; age = 68 ± 10.9 years; male/female = 3/2) and obese (n = 81; BMI = 45.1 ± 1.2 kg/m^2; age = 45 ± 2.2 years; male/female = 26/55) individuals. Indeed, pooling approaches are often used for time- and cost-intensive profiling of different levels of -ome organization including transcriptome,[14,15] proteome,[16] and lipidome (e.g., NIST Standard Reference Material [SRM] 1950 Metabolites in Frozen Human Plasma[6]) characterizations. Here, we created three independent pools per each experimental group by using different subsets of individual samples, allowing the pools to be treated as independent biological replicates. The applied pooling strategy for the description of the reference lipidome has the additional advantage of improving groups discriminative analysis by reducing overall subject-to-subject variation.[17]

Pooled samples were used to test three common extraction protocols (Folch, methyl-*tert*-butyl-ether [MTBE], and hexane/*i*-PrOH/HOAc [Hex/IPA]).[18–20] The most efficient extraction method was chosen based on the recovery of unpolar and polar lipid classes assessed by quantitative high-performance thin-layer chromatography (qHPTLC) and ^{31}P-NMR (Figures 1B, 1C, and S1). Overall, the Folch two-phase extraction protocol was shown to be the most efficient in recovering both unpolar and polar lipids in human WAT.

Even with the optimal extraction, polar lipids represented a minor fraction of WAT lipidome (Figures 1A and 1C). To facilitate deep lipidomic profiling, we performed fractionation of WAT lipid extracts. Lipid fractionation methods utilize differences in molecular motifs or polarity of lipid classes, and here, we compared three orthogonal protocols based on (1) hydrophobicity and ionization state (amino propyl solid phase extraction, SPE; hereafter LipFrac); (2) the presence of phosphodiester groups (zirconia-oxide-based solid phase extraction [Zr-SPE]); and (3) polarity-dependent partitioning between a two-phase solvent system (using liquid-liquid extraction [LLE]). All three protocols showed similar recovery of phosphatidylcholines (PCs), phosphatidylethanoamines (PEs), and sphingomyelines (SMs) lipids (Figure 1D). LipFrac resulted in the highest recovery of free fatty acids (FFAs) but discriminated acidic PLs (e.g., phosphatidylinositols [PIs]) due to their strong binding to the stationary phase. Zr-SPE effectively enriched phosphate-group-containing lipid classes but increased content of lysoPL and FFA due to PL alkaline hydrolysis during the elution step. LLE, based on a partitioning between a hexane and an ethanol/water phase, delivered sufficient enrichment efficiency for all polar lipid classes and was the most time efficient protocol (Figure 1D).

Here, we performed WAT-specific optimization of lipid extraction and fractionation protocols and identified the most efficient sample preparation strategy based on Folch lipid extraction followed by polarity-based LLE, allowing non-discriminative recovery and enrichment of lipids of different classes (Figures 1E and 1F).

WAT lipidome profiling

To increase biological meaningfulness of lipidomics data, lipid annotations should provide information on the lipid class as well as on the discrete fatty acyl chain composition rather than on the total number of carbon atoms and double bond equivalents. Liquid chromatography-tandem mass spectrometry (LC-MS/MS)-based lipidomics allows accurate identification of lipids at the molecular species level (e.g., PC 16:0_18:2), but in complex lipid mixtures with a high dynamic range of lipid concentrations, the coverage of the identified lipidome will depend on the total resolution of the analytical platform. For deep WAT lipidome profiling, we utilized three LC systems, each coupled on-line to high-resolution accurate mass (HRAM) MS/MS (Figure 2A). Highly hydrophobic TG lipids represented by a large diversity of molecular species and a dynamic range of concentrations were separated using C30 reversed-phase LC (RPC), whereas the more polar LLE fraction (PLs, sphingolipids [SLs], diglycerides [DGs]) was resolved using C18 RPC (Figure 2B). Highly polar acyl carnitines (CARs) were separated by hydrophilic interaction LC (HILIC) (Figure 2B), as they are not sufficiently retained on RP columns. Moreover, MS analysis using data-dependent acquisition (DDA) relied on different HRAM platforms and was specifically tailored to enhance identification depth for each targeted lipid class. To this end, C30 RPC-separated TGs were analyzed in positive polarity on a Q Exactive Plus MS with traditional DDA and on an Orbitrap Fusion Lumos Tribrid MS using AcquireX deep scan acquisition workflow for in-depth

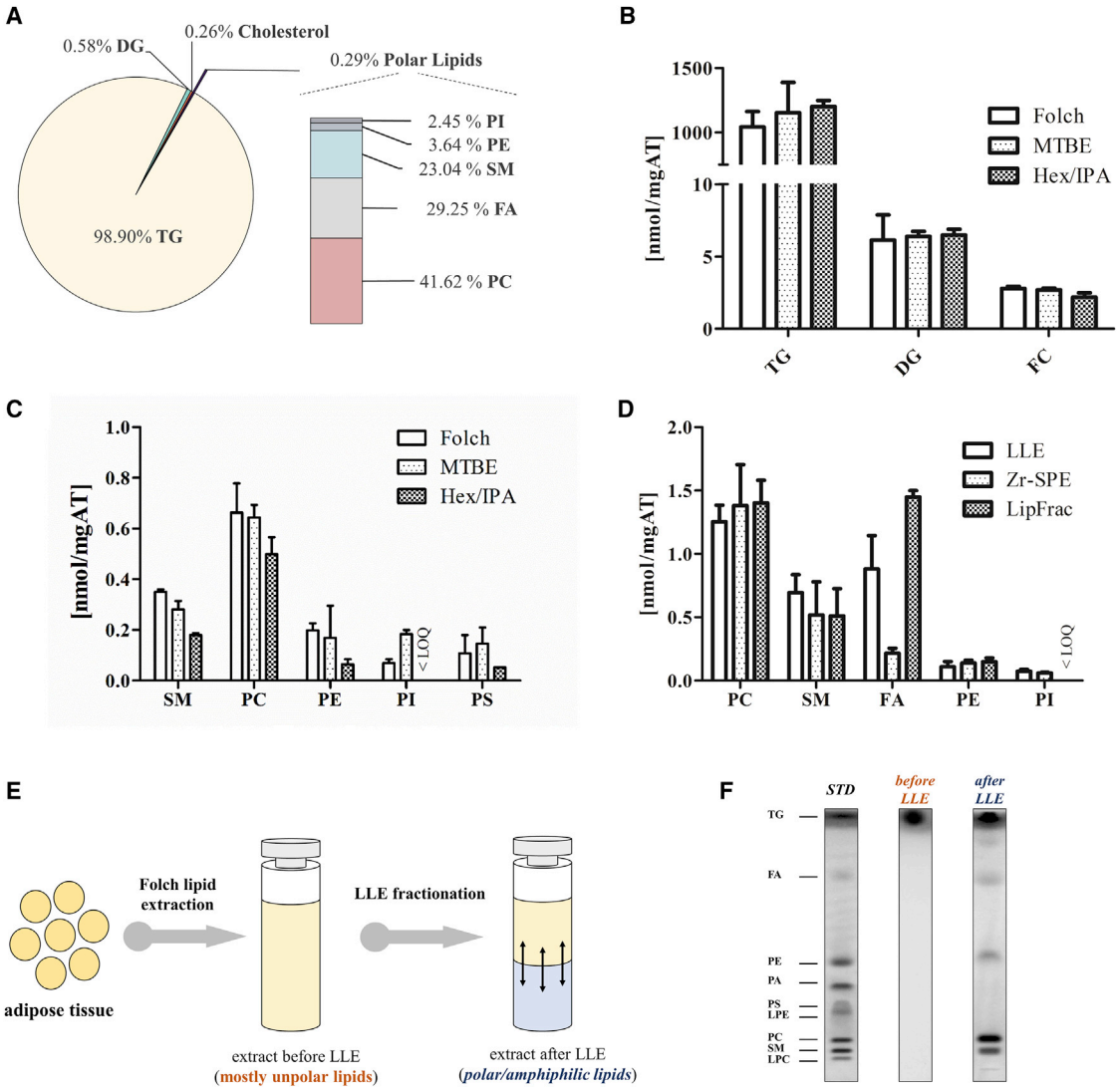

Figure 1. Optimization of sample preparation protocols for global lipidome profiling of human WAT

(A) Lipid-class-specific WAT lipidome composition as determined by quantitative high-performance thin layer chromatography (qHPTLC) of Folch lipid extracts in combination with liquid/liquid extraction (LLE) for polar lipid enrichment.

(B) Extraction efficiency of unpolar lipids as determined by qHPTLC. WAT lipids were extracted by the Folch, the methyl-*tert*-butyl-ether (MTBE), or the hexane/*i*-PrOH/HOAc (Hex/IPA) method.

(C) Extraction efficiency of phosphate containing polar lipids by the different lipid extraction protocols was determined with ^{31}P-NMR.

(D) Efficiency to separate polar and unpolar lipids from WAT lipid extracts was compared using polarity separation by LLE, by separation based on the presence of phosphate groups in lipids by zirconia-oxide-based solid phase extraction (Zr-SPE), or by aminopropyl SPE-based lipid class fractionation (LipFrac).

(E) Schematic depiction of the optimized lipid extraction and fractionation protocol.

(F) qHPTLC analysis of WAT lipidome before (total lipid extract dominated by unpolar lipids) and after (enriched polar and amphiphilic lipids; ethanol fraction) LLE fractionation.

identification of TG molecular species. Less abundant amphiphilic lipids, on the other hand, were detected by DDA on a Q Exactive platform and a Orbitrap Fusion Lumos instrument, both in the positive and the negative modes. As we originally failed to detect any cholesteryl esters (CEs), retinol esters, desmosterol esters, or cardiolipins in WAT total extracts, we set up targeted parallel reaction monitoring (PRM) for the detection of most prominent species. That allowed us to detect seven CEs otherwise masked by highly abundant TGs. However, both retinol and desmosterol esters, as well as cardiolipins, remained undetected in human WAT.

To ensure high-confidence accurate lipid identification, we used three software tools: LipidHunter,[21] LipidSearch, and Lipostar.[22] Obtained results were cross-matched, and the list of putative lipid identifications was manually curated to exclude false-positive identifications. We further validated manually curated lipid annotations by plotting the retention time of a given lipid species against its Kendrick mass defect (KMD) to

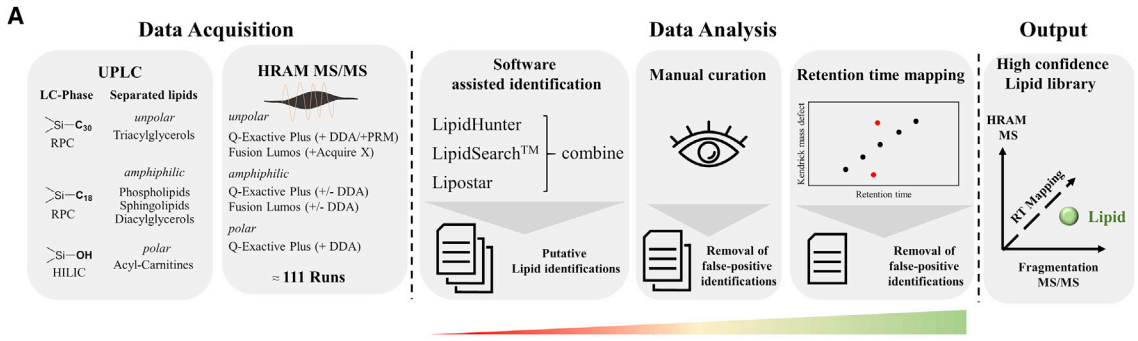

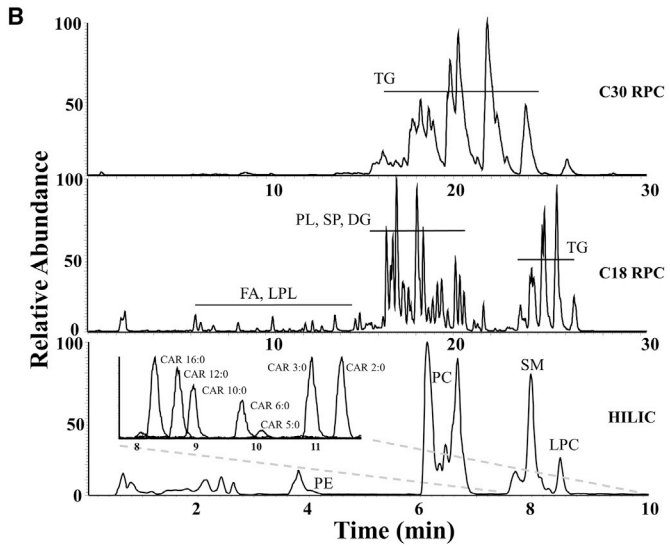

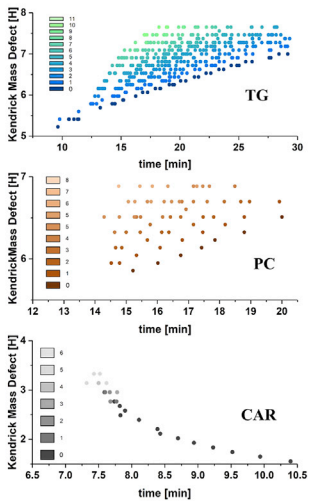

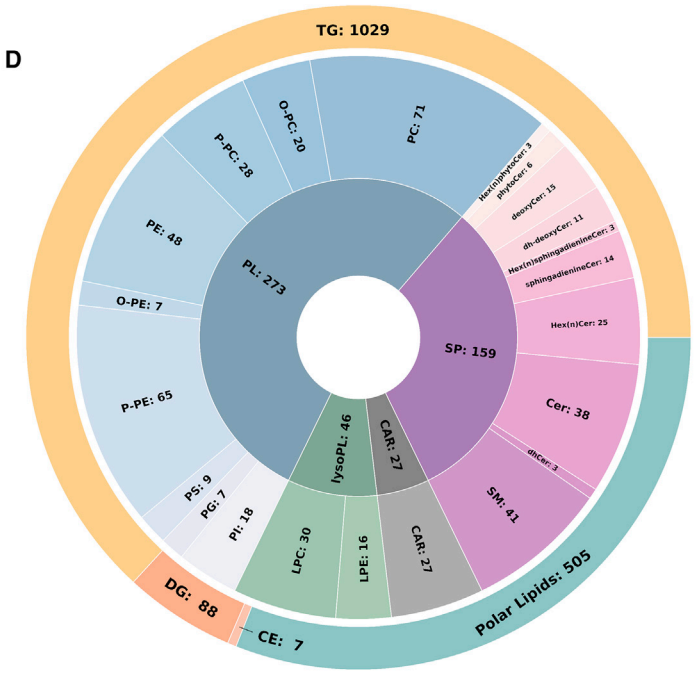

(legend on next page)

the hydrogen base (Figure 2C). Detailed description of manual MS/MS curation and retention time mapping for lipids of different (sub)classes can be found at https://github.com/SysMedOs/AdipoAtlasScripts/blob/main/LipidIdentification/AdipoAtlas_Lipid_Identification_Manual.pdf. In some cases (MG, short acyl chain TG, CAR), coelution with lipid standards was used to validate their identity (Figure S2). Such rigorous curation of lipid annotations allowed us to resolve lipid classes, which are often not discriminated. For instance, using a defined set of specific fragment ions as well as retention time mapping, unambiguous identification of acyl-, alkyl-, and alkenyl-PL, as well as lysoPL, became possible.

Overall, we obtained a list of 1636 lipids representing 23 lipid subclasses (Figure 2D; Table S1). TGs display the highest lipidome complexity, making up 63.2% of all identified lipids followed by PL (16.8%), SP (9.8%), DG (5.4%), lysoPL (2.8%), acylcarnitines (1.7%), and CEs (0.4%). Eventually, we achieved a three-dimensionally curated (RT-MS-MS/MS), high-confidence lipid inventory of human WAT covering all major lipid classes including glycerolipids, PLs, SPs, CEs, and acylcarnitines, representing the most detailed description of human WAT lipidome to date.

Quantitative analysis of human WAT lipidome

The significance of accurate quantification for harmonization of lipidomics data was recently underlined by the lipidomics community.[23] However, several analytical challenges need to be accounted for when aiming for accurate lipid quantification. MS signal intensity is molecular structure dependent and, as such, requires application of internal standards (ISTDs) to support accurate quantification. The highest possible quantitative accuracy can be obtained by using isotopically labeled ISTDs for each molecular species in the sample, which is, unfortunately, still not feasible at the whole-lipidome level. Here, we performed semi-absolute quantification of identified WAT lipids using lipid-subclass-specific ISTDs at concentrations close to the endogenous analytes (Figure 3A). WAT-specific ISTD mixture was designed to cover the whole range of identified lipid classes (Table S2). Next, 6-point calibration curves were generated for each ISTD spiked in the adipose tissue matrix to determine the linear response range (Figures S3 and S4). Final ISTD amounts in the mixture were chosen to represent intensity close to the native lipids of the corresponding lipid class while still displaying a linear behavior of ISTDs in the concentration-response relationship. Pooled WAT samples were spiked with the designed ISTD mixture prior to lipid extraction and fractionation and analyzed using full-scan LC-MS or PRM platforms utilizing three types of LC separations as described above.

All obtained data were corrected for lipid isotopic patterns (type I), incomplete isotopic enrichment of deuterated ISTDs (Figure 3A), and abundances of different ionization adducts (Table S3). Since not only the lipid class, but also the fatty acyl chain composition, in a given lipid will determine its MS response, we defined acyl-chain-specific response factors for the most abundant and diverse WAT lipid class, TG, that were used to increase the quantitative accuracy of TG (Figure S5; Table S4). Thus, using a comprehensive separation strategy coupled to HRAM MS detection and an in-house-designed ISTD mixture customized to WAT, we performed semi-absolute quantification of the human WAT lipidome covering 522 lipid molecular species as well as 215 TGs quantified at the lipid class level, providing the most detailed semi-quantitative mapping of the human adipose tissue lipidome to date (Figure 3B; Table S5).

Adipose tissue lipids span a wide concentration range and display lipid-class-specific fatty acyl signatures

Quantitative analysis of pooled samples of the assessed cohort enables the investigation of the global human adipose tissue lipidome across lean and obese WAT and, thus, provides a general view of the composition of the WAT lipidome. Quantified WAT lipids displayed a huge dynamic range of concentrations from 12 amol/μg protein (CAR 20:5) up to 8 nmol/μg protein (TG 52:2), spanning over eight orders of magnitude (Table S5). Total TG concentration (96.2 nmol/μg protein) within WAT is overarching other lipid classes by two orders of magnitude, resembling their role as energy storage lipids. Importantly, concentrations of individual TG species ranged over five orders of magnitude, showing the molecular-species-dependent abundance, with just the 20 most abundant TGs representing over 71% of the total TG amount. Those top 20 TGs contained primarily saturated and monounsaturated fatty acyl chains, with an average of two double bonds per three acyl chains (Figure 3C). CEs were the second most abundant lipid class, of which CE 20:4 was the most concentrated (Figure 3F).

Unpolar lipids were followed by PCs, PEs, and SMs. Interestingly, PC and PE lipids showed inverted distribution of the corresponding subclasses (Figure 3D). Thus, diacyl-PCs were ≈ 4.5 times more abundant than ether-PCs, whereas ether-PEs were ≈ 3 times more abundant than diacyl-PEs. Specifically, plasmalogen PEs were the most abundant lipid subclass within PE lipids. Closer inspection of the fatty acyl chain distribution revealed class-/subclass-specific differences. For PC lipids, the fatty acyl chain abundance was largely similar among acyl-, alkyl-, and alkenyl-species, whereas for PEs, a higher concentration of polyunsaturated fatty acids (PUFA)-containing alkenyl-PEs (plasmalogens) was observed over diacyl-PEs. Interestingly, plasmalogen lipids were previously reported to be

Figure 2. Workflow adapted for high-confidence lipid identification from human WAT

(A) Schematic depiction of the identification strategy for three-dimensionally curated, high-confidence lipid library of human WAT.

(B) Lipid-class-specific LC separation was applied to allow for the highest possible chromatographic resolution to achieve optimal lipidome coverage. LC-MS chromatograms of unpolar lipids separated by C30 reversed-phase chromatography (RPC), amphiphilic lipids by C18 RPC, and polar acylcarnitines (CAR) by hydrophilic interaction chromatography (HILIC).

(C) Exemplary depiction of retention time mapping for TG, PC, and CAR lipid classes. Kendrick mass defect to the hydrogen base (KMD[H]) was plotted against lipid retention time to increase confidence of lipid identification.

(D) Graphical representation of human WAT lipid molecular species grouped by the corresponding lipid class obtained by high-confidence identification strategy.

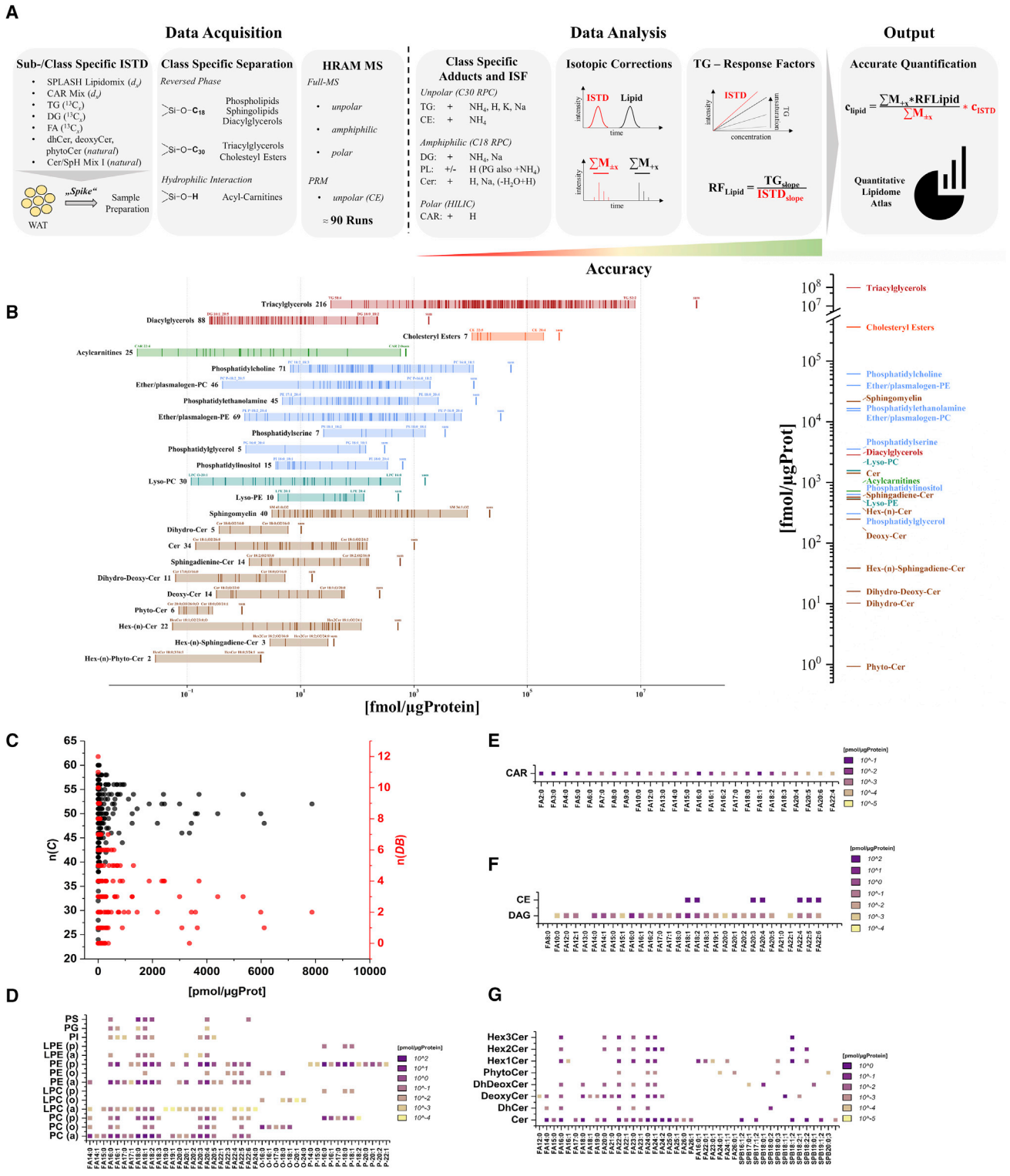

Figure 3. Quantitative representation of human WAT lipidome and description of analytical strategy used

(A) Schematic depiction of the quantitative lipidomics workflow.

(B) Quantitative distribution of lipid class and corresponding lipid molecular species within subclasses of human WAT. Total lipid class concentration is represented by bold lines (*SUM*), and each single lipid molecular species is represented by thin lines.

(legend continued on next page)

enriched in brain and heart tissues. Here, we demonstrate that in human WAT, plasmalogen PEs represent the fourth most abundant lipid class with a total concentration of 11.3 pmol/μg protein, and the most abundant molecular species of plasmalogen PEs are rich in PUFA. LysoPC and lysoPE lipids were one order of magnitude less abundant than PCs and PEs, with acyl chain composition similar to the corresponding diacyl-species, indicating active lipid remodeling within these PL classes via the Lands cycle (Figure 3D). Other PLs were detected only as diacyl species, with PS being the next most abundant class, followed by PIs and PGs. All minor PL lipids showed fatty acyl chain distribution characteristic of those classes.[24,25] Thus, the most abundant PS molecular species were PS 18:0_18:1 and PS 18:0_18:2, whereas PIs were rich in FA 20:4. The most abundant PG was PG 18:1_18:1 (Figure 3D).

DGs and acylCARs displayed quantities in the medium abundance range, illustrating their role as intermediates within lipid metabolism. Indeed, DG acyl chain distribution was quite similar to PLs, indicating the role of DGs as structural precursors of membrane lipids (Figure 3E). The most abundant acylcarnitine was CAR 2:0, in line with its proposed function as a sink for acetyl equivalents that accumulates due to the constant energy surplus to prevent complete coenzyme A (CoA) consumption, especially in highly metabolically active tissues such as WAT (Figure 3E)[26–28]. Other abundant species, CAR 3:0 and CAR 5:0, possibly originate from branched-chain amino acid oxidation.[29,30] Additionally, relatively high concentrations of CAR 16:0, 16:1, 18:0, 18:1, and 18:2 were observed, indicating acylCARs shuttling medium-chain FAs to mitochondrial β-oxidation.[28] This quantitative assessment of CAR species within human WAT further supports its role as a highly metabolically active organ.

Another lipid class of high metabolic importance often implicated in the development of obesity-related pathologies is ceramides (Cers) (Figure 3G). We found preferential incorporation of saturated or monounsaturated long- and very-long-chain FAs in Cer lipids, typical for this lipid class. The most abundant (203 fmol/μg protein) Cer in human WAT was Cer 34:1;O2, represented by two isomeric species: Cer 18:1;O2/16:0 and Cer 16:1;O2/18:0. Cer 18:1;O2/16:0 and corresponding Cer synthase (CerS6) were previously associated with weight gain and glucose intolerance.[31] On the other hand, Cers with sphingoid bases (SPBs) other than SPB 18:1;O2 are rarely monitored and, thus, usually not reported.[31,32] Overall, we demonstrated previously unanticipated diversity of Cer subclasses in human WAT. Cers were represented by species with varying lengths of SPBs, of which SPB 18:1;O2 and SPB 16:1;O2 were the most abundant. Dihydroceramides (dhCer), precursors in *de novo* Cer biosynthesis, were concentrated one order of magnitude lower than Cers themselves. The next most abundant Cer subclass was hexosylated Cer derivatives, closely followed by sphingadienine-Cer, a class of lipids only recently discovered and monitored in human blood plasma.[33] Finally, to our surprise, human WAT was enriched in deoxy-Cer lipids. This potentially cytotoxic Cer subclass was detected in human blood plasma, where it represents a minor (0.1%–0.3%) fraction of total SPBs. Here, WAT contained significant amounts of deoxy-Cer lipids, corresponding to 12.6% of all Cer subclasses. Considering the close interconnection of SP metabolic pathways and already established functional differences of structurally diverse Cer lipids,[32,34] *AdipoAtlas* significantly enriches the current knowledge of the human WAT lipid composition.

PUFA-containing TGs are specifically upregulated in obese WAT

Having a detailed, semi-quantitative map of human WAT in hand, we compared global lipidome compositions of SAT and VAT from lean and obese individuals. As expected, we found a statistically significant upregulation of TGs in obese adipose tissue (Figure 4A). Interestingly, all obesity-upregulated TGs contained at least one PUFA residue, with FA 20:4, FA 20:5, FA 22:5, and FA 22:6 acyl chains being the most upregulated PUFAs in that respect (Figure 4B). Conversely, TG species containing mostly saturated fatty acid and monounsaturated fatty acid residues were markedly decreased in the adipose tissue of obese individuals (Figure 4A). Correlation analysis further confirmed strong co-regulation of PUFA-TG (Figure 4C), indicating that the observed trend is not limited to single lipid species but is a general feature of TGs in obesity. Previously, obesity-driven global accumulation of long-chain PUFA-containing TGs was demonstrated in murine models and human biopsies.[35–38] Increased activity of the FA elongase Elovl6 was proposed to play a role as a common phenomenon in rodent and human adipose tissue in response to excessive nutrient consumption.[38] This suggests that besides upregulation of total enzymatic FA elongation/desaturation machinery, the generation of specific TG molecular species is regulated during obesity development and opens up the questions of how and why specific lipogenic enzymes generate distinct TG species and what their role is in obesity development.

Increase in sphingadienine-containing Cers is a hallmark of obese adipose tissue

Obesity is one of the main risk factors for the development of T2DM, precluded by organ-specific or systemic insulin resistance.[39] Cers are well-known mediators of insulin resistance, with Cer levels in different organs reflecting insulin sensitivity state.[34] Here, in the obese adipose tissue, we found a marked upregulation of Cers with FA 24:1 acyl chains and Cers with the unusual SPB sphingadienine (SPB 18:2;O2) (Figures 4A and 4D). Sphingadienine (SPB 18:2;O2) Cers are a (so far) functionally undescribed class, the synthesis of which has been proposed in adipose tissue but not confirmed until now.[33] Upregulated sphingadienine Cers contained a diverse range of esterified acyl chains (from FA 14:0 up to FA 24:0) (Figure 4D). Correlation analysis showed that there is a strong co-regulation between all upregulated SPB-18:2;O2-containing Cers (Figure 4B), indicating an increased biosynthesis of this unusual SPB or/and an increased acylation rate of the sphingadienine base.

(C) Distribution of single TG based on bulk FA chain length (expressed as total carbon number, n(C); black dots) and unsaturation (expressed as double bond number, n(DB); red dots).
(D–G) Quantitative distribution of FAs, fatty alcohols, fatty vinyl alcohols, and SPBs across (D) PLs, (E) acylCARs, (F) CEs and diacylglycerols and, (G) SPs. Plotted FA concentrations were determined by summing up the concentration of individual species containing a particular fatty acyl chain per lipid subclass.

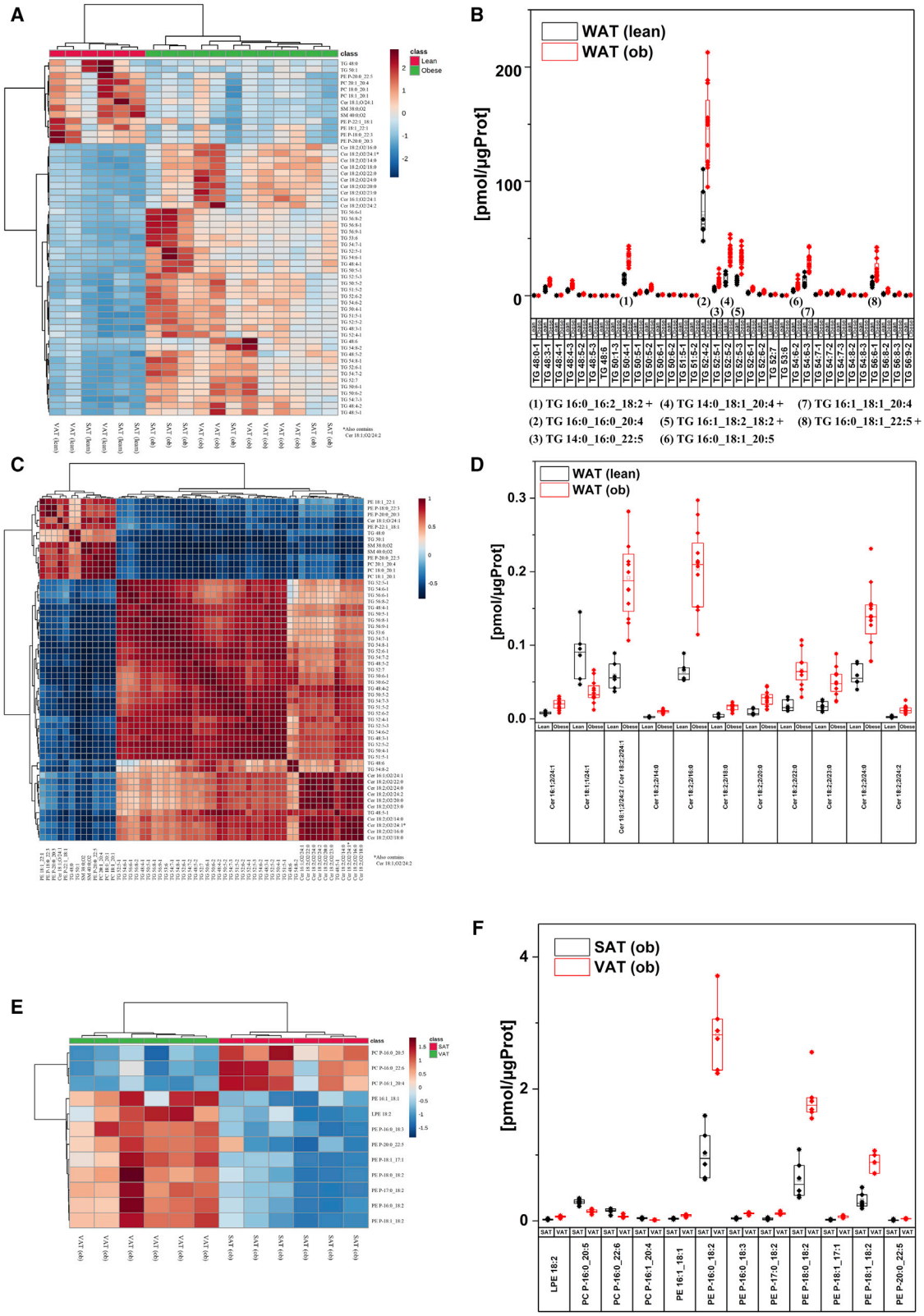

(legend on next page)

Plasmalogen PLs are a depot-specific signature in acquired obesity

Encouraged by the fact that *AdipoAtlas* provided new insights in the lipidomics signature of obese versus lean adipose tissue, we next looked at the possible difference in lipid compositions of obese SAT and VAT depots. Interestingly, a clear discrimination of SAT and VAT depots was possible based on their respective plasmalogen PL signatures (Figure 4E). Thus, higher amounts of plasmalogen PC with long-chain PUFA (e.g., FA 20:4, FA 20:5, FA 22:6) were characteristic of obese SAT, whereas plasmalogen PEs accumulated in obese VAT. The majority of VAT-upregulated plasmalogen PEs carried 18-carbon-long fatty acyl chains (Figure 5B). Differential regulation of plasmalogen PEs was already indicated in previous studies.[37,38,40] Here, we further demonstrated the involvement of plasmalogen PCs and, importantly, fatty acyl specificity within the regulated lipid species.

DISCUSSION

Deep profiling of tissue-specific lipidomes is essential to support our understanding of human biology by elucidating not only tissue-/organ-specific lipid remodeling mechanisms, but also the cross-talk between different tissues, its impact on systemic regulation of the lipid metabolism, and genome-lipid associations.[41] In contrast to robust screening applications necessary for the analysis of large sample cohorts and potential clinical translation, deep lipidomics profiling of a particular tissue, organ, or cell type cannot be performed in a high-throughput manner and requires rigorous tissue-tailored optimizations and application of multiple orthogonal analytical workflows. Here, we provide the example of an analytical strategy targeting deep lipidomic profiling of human WAT, which can be transferred and adapted for the generation of reference lipidomes from any other human tissue. The workflow included three main steps to ensure non-discriminative deep lipidome coverage, providing a qualitative and quantitative inventory of human WAT lipidome:

(1) Tissue-tailored lipid extraction and fractionation to ensure non-discriminative coverage of all lipid (sub)classes was optimized by testing several protocols using qHPTLC as a robust readout method, allowing fast quantitative assessment of extraction and fractionation efficiencies.
(2) Rigorous identification of lipid molecular species was performed by employing multiple separation (C18 RPC, C30 RPC, HILIC) and MS analysis platforms (± DDA, AcquireX, PRM). LC-MS/MS analysis of four sample pools (SAT and VAT from lean and obese individuals) resulted in over 110 datasets used for lipid identification. Importantly, identification was performed using three independent software tools and was followed up by manual curation of MS/MS spectra and retention time mapping. Such a meticulous strategy was rewarded by accurate identification of over 1600 lipid molecular species, including rarely resolved ones. For instance, using specific sets of fragment ions and subclass-specific elution order, unambiguous identification of diacyl-, alkyl-, and alkenyl-PC and PE lipids was achieved. Furthermore, three-dimensional (LC-MS-MS/MS) curation including control for in-source fragmentation artifacts allowed us to uncover the unexpected diversity of the WAT sphingolipidome. To support accurate lipid identification at the molecular species level, we provide here a summary of lipid fragmentation patterns and retention time maps that can be used by other researchers aiming for deep lipidome mapping.
(3) Semi-absolute quantification of human WAT was based on lipid-class-specific ISTDs that were carefully selected to represent the diversity of endogenous lipids. To this end, a tissue-tailored ISTD mixture was designed and validated. Quantitative data were processed using several types of isotopic corrections, adducts, and in-source fragments. Additionally, response factors accounting for the distribution of diverse acyl chains in TG lipids were calculated and applied to enhance the accuracy of the quantification results. That allowed us to provide semi-quantitative values for 23 lipid subclasses and to appreciate the extraordinarily dynamic range of lipid concentrations within and between different lipid subclasses in human WAT.

Human WAT reference lipidome was reconstructed using pooled samples representative of SAT and VAT depots from lean and obese individuals. Although the application of pooled samples limits a detailed assessment of disease-specific lipid alterations, several depot- and phenotype-specific lipid features became apparent. Accumulation of TG lipids in WAT is a known hallmark of obesity. *AdipoAtlas* demonstrated diverse WAT TGs, represented by 1029 molecular species. Interestingly, TGs were also characterized by the largest dynamic range of concentrations, with only 20 TGs covering over 70% of the total TG concentration. Thus, the most abundant TG, 52:2, corresponded to 6.8 μg/μg of AT proteins. Although the top 20 most abundant WAT TGs were mostly saturated (two double bonds per three acyl chains on average), PUFA-rich TG species were significantly upregulated in obese WAT. These results are in line with previous studies illustrating the enrichment of PUFA TG in obese adipose tissue.[37,38] However, mechanistic understanding of such

Figure 4. Human WAT displays distinct lipidome profiles depending on WAT depot (VAT versus SAT) and phenotype (lean versus obese)
The global lipidome was quantified for representative pools of WAT from VAT and SAT depots of lean (n = 5) and obese (n = 81) individuals.
(A) Heatmap displaying statistically significantly regulated lipid molecular species between the WAT of obese and lean patients.
(B) Concentration of differentially regulated triacylglycerols (TGs) between obese and lean WAT.
(C) Pearson correlation of significantly regulated lipids between lean and obese WAT.
(D) Concentration of statistically significantly regulated Cer species between lean and obese WAT.
(E) Heatmap displaying statistically significantly regulated lipid molecular species between obese VAT (VAT[ob]) and obese SAT (SAT[ob]) depots.
(F) Concentrations of PL and plasmalogen PL species that are statistically significantly regulated between VAT(ob) and SAT(ob). Statistical significance was determined by Student's t test (FDR adjusted) with a cutoff of $p \leq 0.05$ and a minimum fold change ≥ 2.

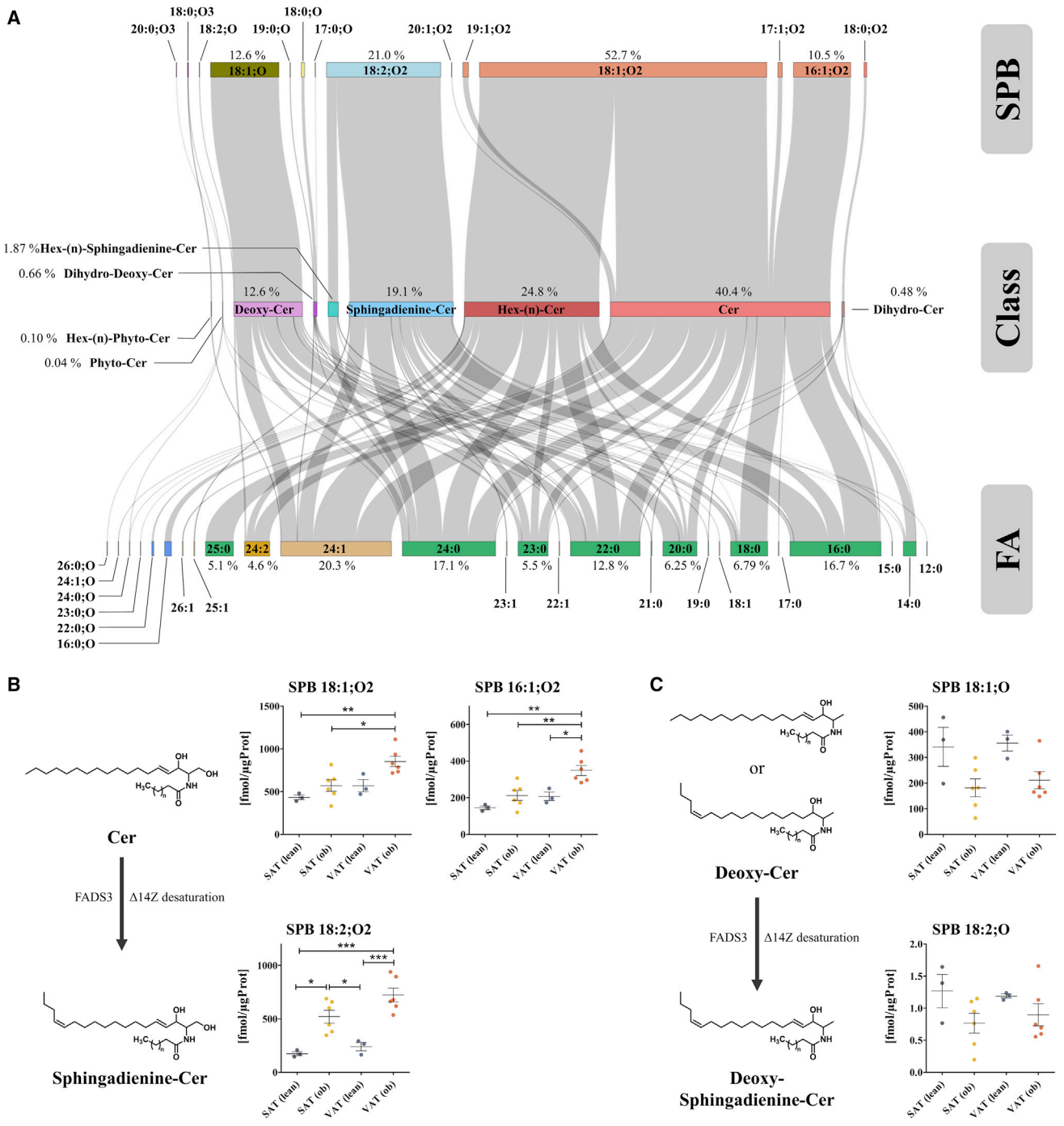

Figure 5. Complexity of the human WAT sphingolipidome

(A) Sankey plot displays the concentration of Cer subclasses, its corresponding esterified SPBs, and FAs. Depicted concentrations were calculated by averaging concentrations of WAT from SAT and VAT depots of lean and obese patients in order to reflect the general WAT sphingolipidome. Length of boxes corresponds to the determined concentrations.

(B) Differential regulation of sphingosine and sphingadienine SPBs over Cer subclasses in obese (ob) and lean tissues from VAT and SAT depots.

(C) Differential regulation of deoxy-sphingosine and deoxy-sphingadienine SPBs over Cer subclasses in obese (ob) and lean tissues from VAT and SAT depots. Statistical significance was calculated by ANOVA. *p ≤ 0.05; **p ≤ 0.01; ***p ≤ 0.005.

specificity remains limited. Using *in vitro* reconstituted artificial lipid droplets (LDs), we recently demonstrated that lipid composition of both the neutral core TGs and the PL monolayer dictates the size of artificial LDs.[42] Interestingly, higher amounts of PUFA-TG lead to the formation of much larger LDs, whereas PUFA-PC had the opposite effect. Thus, it is intriguing to speculate that elevated levels of PUFA-TGs observed in obese WAT might correlate with the larger size of the LDs in hypertrophic adipocytes.

One of the main discoveries provided by *AdipoAtlas* is the previously uncovered diversity of WAT sphingolipidomes. SPs, and especially Cers, recently attracted a lot of scientific attention. Tissues and blood plasma levels of these lipids emerge as important predictors of metabolic malfunction in human pathologies associated with altered lipid metabolism. Cer accumulation was associated with deleterious metabolic outcomes, including insulin resistance, ectopic lipid accumulation, apoptosis, and fibrosis.[43] Cer biosynthesis and catabolic pathways were identified as favorable targets for pharmacological intervention in metabolic diseases. Thus, knockdown or small-molecule-based inhibition of serine palmitoyltransferase (SPTLC), dihydroceramide desaturase 1 (DEGS1), selected isoforms of Cer synthases (CerS), as well as overexpression of ceramidases (acid ceramidase and adiponectin receptor) all showed beneficial effects in metabolically challenged mice.[44–47]

Elevated Cer levels were found in WAT in obesity and obesity-associated diseases including T2DM,[32] fatty liver diseases,[48] and metabolic syndrome.[49] Details on Cer tissue depot specificity (SAT versus VAT) remain less obvious. The majority of the human studies used either SAT or VAT, and reports directly comparing SAT and VAT Cer levels are rare. However, current data indicate the significance of Cer acylated with FA 16:0 as the molecular species associated with adverse metabolic outcomes.[31] This observation is further supported by transcriptomics analyses showing significant upregulation of CerS6, an isoform of Cer synthase preferentially acylating FA 16:0 into Cer, in WAT of obese individuals.[31] It is important to note that most of the studies reporting Cer levels in human WAT utilize targeted detection methods that cover only "classical" species (Cer, dhCer, and sometimes their glycosylated derivatives), in which SPB 18:1;O2 (sphingosine) is acylated with different fatty acyl chains. Using our advanced analytical workflow, we demonstrated that WAT sphingolipidome is more complex, with SPB 18:1;O2 Cer representing only 69.2% of all classical Cers (Figure 5). *AdipoAtlas* facilitated the identification of four additional bases: SPB 16:1;O2 (26.1%), SPB 19:1;O2 (2.6%), SPB 17:1;O2 (2.1%), and SPB 20:1;O2 (0.7%). Both SPB 18:1;O2 and SPB 16:1;O2 were elevated in obese WAT, and their levels were higher in VAT in comparison to SAT of lean and obese origin (Figure 5B). Overall, "classical" Cers represent only 40% of total Cer species quantified in WAT. The next most abundant subclass was glycosylated Cer (25%) containing up to three hexoses (Hex(n)Cer).

Interestingly, we identified two more highly abundant "atypical" Cer classes in human WAT: deoxyCer and sphigadienineCer. DeoxyCers are acylated derivatives of 1-deoxy-sphingosine (SPB 18:0;O), synthesized by SPT from palmitate and alanine instead of serine.[50] They are typically considered as toxic by-products in Cer metabolism, as they can neither be degraded via classical Cer catabolic pathways nor be converted to SM and glycoCer species. DeoxyCers were only recently identified in human adipose tissue, with higher levels in VAT relative to serum, particularly in obese individuals with T2DM.[51] Plasma levels of deoxyCer were positively associated with age, BMI, and waist-to-hip ratio,[52,53] proposing them as a hallmark of metabolic complications. Interestingly, in plasma, SPB 18:1;O represents only a minor (0.1%–0.3%) fraction,[52] whereas *AdipoAtlas* revealed 10-times-higher values in human WAT (12.6%) (Figure 5A). This suggests a significant enrichment of these potentially toxic species in WAT, although the exact role of deoxyCers remains to be uncovered. Previously believed to be mainly of hepatic origin, deoxyCers were shown to be directly synthesized by adipocytes during differentiation.[51] Thus, *AdipoAtlas*, as well as recently reported data,[51] allows us to propose human WAT as an important reservoir and a source of potentially toxic deoxyCer.

SphigadienineCer represented another abundant Cer subclass in human WAT (Figure 5). In comparison to "classical" Cer, sphigadienineCers contain one more double bound at the position Δ14Z (SPB 18:2;O2). Previously, SPB 18:2;O2 Cers were shown to reflect metabolic fitness due to an inverse association with homeostatic model assessment for insulin resistance, BMI, and incidence of cardiovascular events.[54,55] Although the existence of SPB 18:2;O2 has long been known, the enzyme (FA desaturase 3; FADS3) responsible for the introduction of Δ14Z double bond was discovered only recently.[33] According to gene expression data from GTEx portal (https://gtexportal.org/home/index.html), the highest FADS3 expression levels were found in peripheral nerve, aorta, and WAT. Gender-specific expression analysis further unraveled the highest expression of FADS3 in female WAT. So far, sphigadienineCers were not characterized in adipose tissue. Here, we report that they represent 19% of all Cer subclasses within human WAT (Figure 5A). Moreover, 18:2;O2 Cers were elevated in both SAT and VAT obese depots with significant enrichment of this lipid class in VAT versus SAT. Importantly, elevated levels of 18:2;O2 Cers represented a specific signature of obese WAT, showing statistical significance even for the pooled samples utilized in this study (Figure 4D). Although depot- and phenotype-specific increase in sphigadienineCer displayed the trend similar to Cer, their fatty acyl chain distribution was somewhat different, with a lower portion of FA 18:0 acylated into 18:2;O2 Cer in comparison to 18:1;O2 Cer. Our results strongly suggest that sphingadieneCer accumulation is a hallmark of obesity. Previously published data showed significant gender specificity for deoxy- and sphigadienineCer subclasses, with SPB 18:2;O being more abundant in men and SPB 18:2;O2 Cer in women. Interestingly, we observed an inverse correlation between those lipid classes in lean and obese WAT (Figure 5B), which might be explained by 2/3 prevalence of female WAT donors in our sample pools. Further analysis of individual samples based on the *AdipoAtlas* list will provide deeper insights into gender- and disease-specific signatures of Cer lipids.

Another emerging class of lipids potentially involved in the regulation of cellular and systemic lipid homeostasis is etherPL (ePL), including plasmalogens (pPL). Previously, brain and heart were identified to be rich in pPL. *AdipoAtlas* showed that ePC

and ePE lipids composed 41% of total PCs and PEs. Specifically, we demonstrated that PUFA-rich ePE (40 pmol/μg protein) represented the fourth most abundant lipid class in human WAT, closely following the most abundant PC PLs (62 pmol/μg protein). We identified depot-specific signatures of ePLs with higher levels of PUFA pPCs in SAT and enrichment of C18 fatty acyl chain containing pPEs in VAT. Ether lipids, and plasmalogens especially, play a central role in lipid quality control, adaptive responses to the change in lipid saturation levels, and maintenance of membrane fluidity.[56] pPEs compose over 20% of inner leaflets of the plasma membrane,[57] making them important players in membrane remodeling during adipocyte hypertrophic growth.[37] Moreover, levels of circulating plasmalogens were inversely associated with hypertension, prediabetes, T2DM, cardiovascular diseases, and obesity.[24] Interestingly, inverse co-regulation of ether lipids and SPs was recently demonstrated, with depletion of ePL leading to the Cer accumulation and vice versa.[58] *AdipoAtlas* provides an inventory of ePL molecular species including resolved diacyl-, alkyl-, and alkenyl-PLs, which can be used as a resource for close, targeted follow up of this inverse correlation in larger sample cohorts.

However, one should note that many of the observed changes might reflect adaptive, rather than maladaptive, mechanisms employed by WAT to escape lipotoxicity. Indeed, it is likely that many toxic, maladaptive effects observed in obesity and other metabolic disorders might be a result of the initially adaptive responses failed under the chronic metabolic burden. For instance, reported lipotoxic effects of Cers should be seen in the perspective of metabolic malfunction, deriving from dysregulation of Cer metabolism rather than original Cer function. Indeed, in conditions of energy oversupply and constantly increasing flux of FFAs, Cers play an important role in preventing uncontrolled distribution of lipotoxic FFAs characterized by detergent-like (membrane lysis) activities. Cers were reported to promote safe FFA translocation via CD36 and to increase FFA incorporation into TGs by increasing TG synthesis and decreasing lipolysis rates.[59] Cers are also linked with decrease in mitochondrial efficiency, possibly via induction of mitochondrial fission, leading to higher consumption of FA substrates per unit of ATP production and thus allowing cells to utilize higher amounts of FAs at the condition of excess energy supply. The role of Cers in inhibition of insulin signaling is usually seen as a negative effect. However, it is interesting to speculate that the initial effect of Cers on the inhibition of Akt signaling via protein kinase C zeta and protein phosphatase 2A, leading to "selective" insulin resistance in response to glucose, is an adaptive mechanism further promoting FFA utilization. The adaptive role of Cer synthesis in the condition of FFA oversupply is additionally supported by the presence of regulatory feedback loops.[59] Thus, controlled activation of lipolysis via β-adrenergic stimulation and adiponectin signaling leads to the inhibition of Cer synthesis and increases their degradation, respectively. However, in conditions of continuous oversupply of FFAs (energy-rich diet and increased *de novo* lipogenesis), adaptive Cer signaling and its feedback regulation will fail, leading to "full" insulin resistance, pro-inflammatory signaling, and, ultimately, apoptosis as the last option of defense and safe disposal of overwhelming amounts of detergent-like FFA.

Overall, deep lipidomic profiling allowed us to reconstruct human WAT reference lipidome. *AdipoAtlas* provides an inventory of over 1600 lipid molecular species from 23 lipid (sub)classes fortified by their semi-quantitative values in two WAT depots (SAT and VAT) from lean and obese individuals. That allowed us to demonstrate an amazing diversity of adipose tissue lipids together with an assessment of their quantities between and within lipid classes. Several important lipid signatures characteristic of obesity were discovered or reproduced, pointing out the qualitative and quantitative accuracy of the applied methodology. *AdipoAtlas* is freely available for all researchers interested in WAT biology and can be further used to design human-WAT-specific high-throughput experiments targeting quantification of any given lipid (sub)class in large sample cohorts. Moreover, *AdipoAtlas* will provide currently missing scaffolding for systems biology integration of lipidomics data via reconstruction of lipid-centric genome scale metabolic models, linking big omics data with identification of disease characteristic metabolic, and signaling pathways.

Limitations of the study

Tissue pools used in the study proved to be useful for in-depth characterization of human WAT lipidome. However, this reference lipidome does not account for the age and gender variability within human populations. Furthermore, data on the inter- and even intra- (longitudinal) individual variability need to be provided in the future to reflect WAT remodeling upon obesity development. Measurement of WAT lipidomes in individual samples using large clinical cohorts has to be performed to address these limitations. Further integration of lipidomics data with transcriptomics and/or proteomics results will amplify the utility of *AdipoAtlas* as a resource.

STAR★METHODS

Detailed methods are provided in the online version of this paper and include the following:

- KEY RESOURCES TABLE
- RESOURCE AVAILABILITY
  - Lead contact
  - Materials availability
  - Data and code availability
- EXPERIMENTAL MODEL AND SUBJECT DETAILS
- METHOD DETAILS
  - Sample preparation
  - Lipid extraction
  - Lipid fractionation
  - Quantitative high performance thin layer chromatography (qHPTLC)
  - Chromatography
  - Data dependent acquisition on Q Exactive Plus Hybrid Quadrupole Orbitrap mass spectrometer
  - Data dependent acquisition on Orbitrap Fusion Lumos Tribrid mass spectrometer
  - Acquire X on Orbitrap Fusion Lumos Tribrid mass spectrometer for in-depth triacylglycerol identification
  - Targeted identification of cholesteryl esters
  - Co-elution of short chain TGs, MGs, and acylcarnitine's with corresponding internal standards
  - Lipid identification

- LipidSearch
- LipidHunter[21]
- Lipostar[22]
- Merge of identification results
- Manual lipid annotation
- Lipid quantification

- QUANTIFICATION AND STATISTICAL ANALYSIS
  - Response factors calculations for triacylglycerols
  - Software

SUPPLEMENTAL INFORMATION

Supplemental information can be found online at https://doi.org/10.1016/j.xcrm.2021.100407.

ACKNOWLEDGMENTS

Financial support from the German Federal Ministry of Education and Research (BMBF) within the framework of the e:Med research and funding concept for the SysMedOS project (to M.F.) are gratefully acknowledged. We thank Prof. Ralf Hoffmann (Institute of Bioanalytical Chemistry, University of Leipzig) for providing access to his laboratory.

AUTHOR CONTRIBUTIONS

M.F. conceived the project, guided the research, assisted with the experiments and data interpretation, and wrote the manuscript. M.L. designed and performed most of the experiments, analyzed and interpreted data, and wrote the manuscript. G.A. performed lipid identification, including manual annotation and retention time mapping. Z.N. performed lipid identification and dataset merging and prepared the illustrations. A.C. performed parts of the LC-MS/MS experiments. J.S. assisted with ^{31}P NMR and analysis of lipids from TLC plates. M.B. provided human WAT samples. All authors edited and approved the manuscript.

DECLARATION OF INTERESTS

M.B. received honoraria as a consultant and speaker from Amgen, AstraZeneca, Bayer, Boehringer-Ingelheim, Lilly, Novo Nordisk, Novartis, and Sanofi. All other authors declare no competing interests.

Received: March 11, 2021
Revised: July 29, 2021
Accepted: August 26, 2021
Published: September 22, 2021

REFERENCES

1. Uhlén, M., Fagerberg, L., Hallström, B.M., Lindskog, C., Oksvold, P., Mardinoglu, A., Sivertsson, Å., Kampf, C., Sjöstedt, E., Asplund, A., et al. (2015). Tissue-based map of the human proteome. Science *347*, 1260419.
2. Huynh, K., Barlow, C.K., Jayawardana, K.S., Weir, J.M., Mellett, N.A., Cinel, M., Magliano, D.J., Shaw, J.E., Drew, B.G., and Meikle, P.J. (2019). High-Throughput Plasma Lipidomics: Detailed Mapping of the Associations with Cardiometabolic Risk Factors. Cell Chem. Biol. *26*, 71–84.e4.
3. Seah, J.Y.H., Chew, W.S., Torta, F., Khoo, C.M., Wenk, M.R., Herr, D.R., Choi, H., Tai, E.S., and van Dam, R.M. (2020). Plasma sphingolipids and risk of cardiovascular diseases: a large-scale lipidomic analysis. Metabolomics *16*, 89.
4. Frayn, K.N., Arner, P., and Yki-Järvinen, H. (2006). Fatty acid metabolism in adipose tissue, muscle and liver in health and disease. Essays Biochem. *42*, 89–103.
5. Furse, S., Fernandez-Twinn, D.S., Jenkins, B., Meek, C.L., Williams, H.E.L., Smith, G.C.S., Charnock-Jones, D.S., Ozanne, S.E., and Koulman, A. (2020). A high-throughput platform for detailed lipidomic analysis of a range of mouse and human tissues. Anal. Bioanal. Chem. *412*, 2851–2862.
6. Bowden, J.A., Heckert, A., Ulmer, C.Z., Jones, C.M., Koelmel, J.P., Abdullah, L., Ahonen, L., Alnouti, Y., Armando, A.M., Asara, J.M., et al. (2017). Harmonizing lipidomics: NIST interlaboratory comparison exercise for lipidomics using SRM 1950-Metabolites in Frozen Human Plasma. J. Lipid Res. *58*, 2275–2288.
7. Burla, B., Arita, M., Arita, M., Bendt, A.K., Cazenave-Gassiot, A., Dennis, E.A., Ekroos, K., Han, X., Ikeda, K., Liebisch, G., et al. (2018). MS-based lipidomics of human blood plasma: a community-initiated position paper to develop accepted guidelines. J. Lipid Res. *59*, 2001–2017.
8. Criscuolo, A., Zeller, M., Cook, K., Angelidou, G., and Fedorova, M. (2019). Rational selection of reverse phase columns for high throughput LC-MS lipidomics. Chem. Phys. Lipids *221*, 120–127.
9. Blüher, M. (2019). Obesity: global epidemiology and pathogenesis. Nat. Rev. Endocrinol. *15*, 288–298.
10. Raulerson, C.K., Ko, A., Kidd, J.C., Currin, K.W., Brotman, S.M., Cannon, M.E., Wu, Y., Spracklen, C.N., Jackson, A.U., Stringham, H.M., et al. (2019). Adipose Tissue Gene Expression Associations Reveal Hundreds of Candidate Genes for Cardiometabolic Traits. Am. J. Hum. Genet. *105*, 773–787.
11. Haffa, M., Holowatyj, A.N., Kratz, M., Toth, R., Benner, A., Gigic, B., Habermann, N., Schrotz-King, P., Böhm, J., Brenner, H., et al. (2019). Transcriptome Profiling of Adipose Tissue Reveals Depot-Specific Metabolic Alterations Among Patients with Colorectal Cancer. J. Clin. Endocrinol. Metab. *104*, 5225–5237.
12. Martínez, J.A., Milagro, F.I., Claycombe, K.J., and Schalinske, K.L. (2014). Epigenetics in adipose tissue, obesity, weight loss, and diabetes. Adv. Nutr. *5*, 71–81.
13. Gómez-Serrano, M., Camafeita, E., García-Santos, E., López, J.A., Rubio, M.A., Sánchez-Pernaute, A., Torres, A., Vázquez, J., and Peral, B. (2016). Proteome-wide alterations on adipose tissue from obese patients as age-, diabetes- and gender-specific hallmarks. Sci. Rep. *6*, 25756.
14. Assefa, A.T., Vandesompele, J., and Thas, O. (2020). Correction to: On the utility of RNA sample pooling to optimize cost and statistical power in RNA sequencing experiments. BMC Genomics *21*, 384.
15. Peng, X., Wood, C.L., Blalock, E.M., Chen, K.C., Landfield, P.W., and Stromberg, A.J. (2003). Statistical implications of pooling RNA samples for microarray experiments. BMC Bioinformatics *4*, 26.
16. Linscheid, N., Santos, A., Poulsen, P.C., Mills, R.W., Calloe, K., Leurs, U., Ye, J.Z., Stolte, C., Thomsen, M.B., Bentzen, B.H., et al. (2021). Quantitative proteome comparison of human hearts with those of model organisms. PLoS Biol. *19*, e3001144.
17. Oberg, A.L., and Vitek, O. (2009). Statistical design of quantitative mass spectrometry-based proteomic experiments. J. Proteome Res. *8*, 2144–2156.
18. Iverson, S.J., Lang, S.L.C., and Cooper, M.H. (2001). Comparison of the Bligh and Dyer and Folch methods for total lipid determination in a broad range of marine tissue. Lipids *36*, 1283–1287.
19. Matyash, V., Liebisch, G., Kurzchalia, T.V., Shevchenko, A., and Schwudke, D. (2008). Lipid extraction by methyl-tert-butyl ether for high-throughput lipidomics. J. Lipid Res. *49*, 1137–1146.
20. Slatter, D.A., Aldrovandi, M., O'Connor, A., Allen, S.M., Brasher, C.J., Murphy, R.C., Mecklemann, S., Ravi, S., Darley-Usmar, V., and O'Donnell, V.B. (2016). Mapping the Human Platelet Lipidome Reveals Cytosolic Phospholipase A2 as a Regulator of Mitochondrial Bioenergetics during Activation. Cell Metab. *23*, 930–944.
21. Ni, Z., Angelidou, G., Lange, M., Hoffmann, R., and Fedorova, M. (2017). LipidHunter Identifies Phospholipids by High-Throughput Processing of LC-MS and Shotgun Lipidomics Datasets. Anal. Chem. *89*, 8800–8807.

22. Goracci, L., Tortorella, S., Tiberi, P., Pellegrino, R.M., Di Veroli, A., Valeri, A., and Cruciani, G. (2017). Lipostar, a Comprehensive Platform-Neutral Cheminformatics Tool for Lipidomics. Anal. Chem. *89*, 6257–6264.

23. Liebisch, G., Ahrends, R., Arita, M., Arita, M., Bowden, J.A., Ejsing, C.S., Griffiths, W.J., Holčapek, M., Köfeler, H., Mitchell, T.W., et al.; Lipidomics Standards Initiative Consortium (2019). Lipidomics needs more standardization. Nat. Metab. *1*, 745–747.

24. Paul, S., Lancaster, G.I., and Meikle, P.J. (2019). Plasmalogens: A potential therapeutic target for neurodegenerative and cardiometabolic disease. Prog. Lipid Res. *74*, 186–195.

25. Skotland, T., and Sandvig, K. (2019). The role of PS 18:0/18:1 in membrane function. Nat. Commun. *10*, 2752.

26. Ramsay, R.R., Gandour, R.D., and van der Leij, F.R. (2001). Molecular enzymology of carnitine transfer and transport. Biochim. Biophys. Acta *1546*, 21–43.

27. Lopaschuk, G.D., Belke, D.D., Gamble, J., Itoi, T., and Schönekess, B.O. (1994). Regulation of fatty acid oxidation in the mammalian heart in health and disease. Biochim. Biophys. Acta *1213*, 263–276.

28. Schooneman, M.G., Vaz, F.M., Houten, S.M., and Soeters, M.R. (2013). Acylcarnitines: reflecting or inflicting insulin resistance? Diabetes *62*, 1–8.

29. Newgard, C.B., An, J., Bain, J.R., Muehlbauer, M.J., Stevens, R.D., Lien, L.F., Haqq, A.M., Shah, S.H., Arlotto, M., Slentz, C.A., et al. (2009). A branched-chain amino acid-related metabolic signature that differentiates obese and lean humans and contributes to insulin resistance. Cell Metab. *9*, 311–326.

30. Newgard, C.B. (2012). Interplay between lipids and branched-chain amino acids in development of insulin resistance. Cell Metab. *15*, 606–614.

31. Turpin, S.M., Nicholls, H.T., Willmes, D.M., Mourier, A., Brodesser, S., Wunderlich, C.M., Mauer, J., Xu, E., Hammerschmidt, P., Brönneke, H.S., et al. (2014). Obesity-induced CerS6-dependent C16:0 ceramide production promotes weight gain and glucose intolerance. Cell Metab. *20*, 678–686.

32. Chaurasia, B., Kaddai, V.A., Lancaster, G.I., Henstridge, D.C., Sriram, S., Galam, D.L.A., Gopalan, V., Prakash, K.N.B., Velan, S.S., Bulchand, S., et al. (2016). Adipocyte Ceramides Regulate Subcutaneous Adipose Browning, Inflammation, and Metabolism. Cell Metab. *24*, 820–834.

33. Karsai, G., Lone, M., Kutalik, Z., Brenna, J.T., Li, H., Pan, D., von Eckardstein, A., and Hornemann, T. (2020). FADS3 is a Δ14Z sphingoid base desaturase that contributes to gender differences in the human plasma sphingolipidome. J. Biol. Chem. *295*, 1889–1897.

34. Sokolowska, E., and Blachnio-Zabielska, A. (2019). The Role of Ceramides in Insulin Resistance. Front. Endocrinol. (Lausanne) *10*, 577.

35. Grzybek, M., Palladini, A., Alexaki, V.I., Surma, M.A., Simons, K., Chavakis, T., Klose, C., and Coskun, Ü. (2019). Comprehensive and quantitative analysis of white and brown adipose tissue by shotgun lipidomics. Mol. Metab. *22*, 12–20.

36. Cao, H., Gerhold, K., Mayers, J.R., Wiest, M.M., Watkins, S.M., and Hotamisligil, G.S. (2008). Identification of a lipokine, a lipid hormone linking adipose tissue to systemic metabolism. Cell *134*, 933–944.

37. Pietiläinen, K.H., Róg, T., Seppänen-Laakso, T., Virtue, S., Gopalacharyulu, P., Tang, J., Rodriguez-Cuenca, S., Maciejewski, A., Naukkarinen, J., Ruskeepää, A.L., et al. (2011). Association of lipidome remodeling in the adipocyte membrane with acquired obesity in humans. PLoS Biol. *9*, e1000623.

38. Liesenfeld, D.B., Grapov, D., Fahrmann, J.F., Salou, M., Scherer, D., Toth, R., Habermann, N., Böhm, J., Schrotz-King, P., Gigic, B., et al. (2015). Metabolomics and transcriptomics identify pathway differences between visceral and subcutaneous adipose tissue in colorectal cancer patients: the ColoCare study. Am. J. Clin. Nutr. *102*, 433–443.

39. Wondmkun, Y.T. (2020). Obesity, insulin resistance, and type 2 diabetes: Associations and therapeutic implications. Diabetes Metab. Syndr. Obes. *13*, 3611–3616.

40. Barchuk, M., Dutour, A., Ancel, P., Svilar, L., Miksztowicz, V., Lopez, G., Rubio, M., Schreier, L., Nogueira, J.P., Valéro, R., et al. (2020). Untargeted lipidomics reveals a specific enrichment in plasmalogens in epicardial adipose tissue and a specific signature in coronary artery disease. Arterioscler. Thromb. Vasc. Biol. *40*, 986–1000.

41. Linke, V., Overmyer, K.A., Miller, I.J., Brademan, D.R., Hutchins, P.D., Trujillo, E.A., Reddy, T.R., Russell, J.D., Cushing, E.M., Schueler, K.L., et al. (2020). A large-scale genome-lipid association map guides lipid identification. Nat. Metab. *2*, 1149–1162.

42. Lange, M., Wagner, P.V., and Fedorova, M. (2021). Lipid composition dictates the rate of lipid peroxidation in artificial lipid droplets. Free Radic. Res., 1–12.

43. Turpin-Nolan, S.M., and Brüning, J.C. (2020). The role of ceramides in metabolic disorders: when size and localization matters. Nat. Rev. Endocrinol. *16*, 224–233.

44. Chaurasia, B., Tippetts, T.S., Monibas, R.M., Liu, J., Li, Y., Wang, L., Wilkerson, J.L., Rufus Sweeney, C., Pereira, R.F., Sumida, D.H., et al. (2019). Targeting a ceramide double bond improves insulin resistance and hepatic steatosis. Science *365*, 386–392.

45. Correnti, J.M., Juskeviciute, E., Swarup, A., and Hoek, J.B. (2014). Pharmacological ceramide reduction alleviates alcohol-induced steatosis and hepatomegaly in adiponectin knockout mice. Am. J. Physiol. Gastrointest. Liver Physiol. *306*, G959–G973.

46. Glaros, E.N., Kim, W.S., Quinn, C.M., Jessup, W., Rye, K.A., and Garner, B. (2008). Myriocin slows the progression of established atherosclerotic lesions in apolipoprotein E gene knockout mice. J. Lipid Res. *49*, 324–331.

47. Holland, W.L., Brozinick, J.T., Wang, L.P., Hawkins, E.D., Sargent, K.M., Liu, Y., Narra, K., Hoehn, K.L., Knotts, T.A., Siesky, A., et al. (2007). Inhibition of ceramide synthesis ameliorates glucocorticoid-, saturated-fat-, and obesity-induced insulin resistance. Cell Metab. *5*, 167–179.

48. Kolak, M., Westerbacka, J., Velagapudi, V.R., Wågsäter, D., Yetukuri, L., Makkonen, J., Rissanen, A., Häkkinen, A.M., Lindell, M., Bergholm, R., et al. (2007). Adipose tissue inflammation and increased ceramide content characterize subjects with high liver fat content independent of obesity. Diabetes *56*, 1960–1968.

49. Choromańska, B., Myśliwiec, P., Razak Hady, H., Dadan, J., Myśliwiec, H., Chabowski, A., and Mikłosz, A. (2019). Metabolic Syndrome is Associated with Ceramide Accumulation in Visceral Adipose Tissue of Women with Morbid Obesity. Obesity (Silver Spring) *27*, 444–453.

50. Duan, J., and Merrill, A.H., Jr. (2015). 1-deoxysphingolipids encountered exogenously and made de novo: Dangerous mysteries inside an enigma. J. Biol. Chem. *290*, 15380–15389.

51. Hannich, J.T., Loizides-Mangold, U., Sinturel, F., Harayama, T., Vandereycken, B., Saini, C., Gosselin, P., Brulhart-Meynet, M., Robert, M., Chanon, S., et al. (2021). Ether lipids, sphingolipids, and toxic 1-deoxyceramides as hallmarks for lean and obese type 2 diabetic patients. Acta Physiol. (Oxf.) *232*, e13610.

52. Othman, A., Rütti, M.F., Ernst, D., Saely, C.H., Rein, P., Drexel, H., Porretta-Serapiglia, C., Lauria, G., Bianchi, R., von Eckardstein, A., and Hornemann, T. (2012). Plasma deoxysphingolipids: a novel class of biomarkers for the metabolic syndrome? Diabetologia *55*, 421–431.

53. Beyene, H.B., Olshansky, G., Smith, A.A.T., Giles, C., Huynh, K., Cinel, M., Mellett, N.A., Cadby, G., Hung, J., Hui, J., et al. (2020). High-coverage plasma lipidomics reveals novel sex-specific lipidomic fingerprints of age and BMI: Evidence from two large population cohort studies. PLoS Biol. *18*, e3001049.

54. Othman, A., Saely, C.H., Muendlein, A., Vonbank, A., Drexel, H., von Eckardstein, A., and Hornemann, T. (2015). Plasma C20-Sphingolipids predict cardiovascular events independently from conventional cardiovascular risk factors in patients undergoing coronary angiography. Atherosclerosis *240*, 216–221.

55. Chew, W.S., Torta, F., Ji, S., Choi, H., Begum, H., Sim, X., Khoo, C.M., Khoo, E.Y.H., Ong, W.Y., Van Dam, R.M., et al. (2019). Large-scale

lipidomics identifies associations between plasma sphingolipids and T2DM incidence. JCI Insight *5*, 4.

56. Jiménez-Rojo, N., and Riezman, H. (2019). On the road to unraveling the molecular functions of ether lipids. FEBS Lett. *593*, 2378–2389.

57. Lorent, J.H., Levental, K.R., Ganesan, L., Rivera-Longsworth, G., Sezgin, E., Doktorova, M., Lyman, E., and Levental, I. (2020). Plasma membranes are asymmetric in lipid unsaturation, packing and protein shape. Nat. Chem. Biol. *16*, 644–652.

58. Jiménez-Rojo, N., Leonetti, M.D., Zoni, V., Colom, A., Feng, S., Iyengar, N.R., Matile, S., Roux, A., Vanni, S., Weissman, J.S., and Riezman, H. (2020). Conserved Functions of Ether Lipids and Sphingolipids in the Early Secretory Pathway. Curr. Biol. *30*, 3775–3787.e7.

59. Summers, S.A., Chaurasia, B., and Holland, W.L. (2019). Metabolic Messengers: ceramides. Nat. Metab. *1*, 1051–1058.

60. Chong, J., Wishart, D.S., and Xia, J. (2019). Using MetaboAnalyst 4.0 for Comprehensive and Integrative Metabolomics Data Analysis. Curr. Protoc. Bioinformatics *68*, e86.

61. Bradford, M.M. (1976). A rapid and sensitive method for the quantitation of microgram quantities of protein utilizing the principle of protein-dye binding. Anal. Biochem. *72*, 248–254.

62. Galanos, D.S., and Kapoulas, V.M. (1965). Preparation and Analysis of Lipid Extracts from Milk and Other Tissues. Biochim. Biophys. Acta *98*, 278–292.

63. Xiaoning, L., and Michael, Y. (2010). Enrichment of Phospholipids in Biological Samples Using HybridSPE-PL. Reporter US *28.3*, 6–7.

64. Kim, H.Y., and Salem, N., Jr. (1990). Separation of lipid classes by solid phase extraction. J. Lipid Res. *31*, 2285–2289.

65. Dannenberger, D., Süss, R., Teuber, K., Fuchs, B., Nuernberg, K., and Schiller, J. (2010). The intact muscle lipid composition of bulls: an investigation by MALDI-TOF MS and 31P NMR. Chem. Phys. Lipids *163*, 157–164.

66. Schiller, J., Muller, M., Fuchs, B., Arnold, K., and Huster, D. (2007). 31P NMR Spectroscopy of Phospholipids: From Micelles to Membranes. Curr. Anal. Chem. *3*, 283–301.

67. Lísa, M., Cífková, E., Khalikova, M., Ovčačíková, M., and Holčapek, M. (2017). Lipidomic analysis of biological samples: Comparison of liquid chromatography, supercritical fluid chromatography and direct infusion mass spectrometry methods. J. Chromatogr. A *1525*, 96–108.

68. Lange, M., and Fedorova, M. (2020). Evaluation of lipid quantification accuracy using HILIC and RPLC MS on the example of NIST® SRM® 1950 metabolites in human plasma. Anal. Bioanal. Chem. *412*, 3573–3584.

STAR★METHODS

KEY RESOURCES TABLE

REAGENT or RESOURCE	SOURCE	IDENTIFIER
Lipids		
Cer/Sph Mixture I	Avanti Polar Lipids Inc.	LM6002-1EA
Cer 18:0;O3/16:0	Avanti Polar Lipids Inc.	860617P
Cer 18:0;O3/8:0	Avanti Polar Lipids Inc.	860609P
Cer 18:0;O2/8:0	Sigma Aldrich	C8605
Cer 18:0;O2/12:0	Avanti Polar Lipids Inc.	860635
Cer 18:1;O2/17:0,O[2R-OH]	Avanti Polar Lipids Inc.	860817P
Cer 18:1;O/6:0	Cayman Chemical	Cay25493-500
SPLASH® LIPIDOMIX®	Avanti Polar Lipids Inc.	330707-1EA
PC 16:0/18:1	Avanti Polar Lipids Inc.	850457
PE 16:0/18:1	Avanti Polar Lipids Inc.	850757
LPC 18:1	Avanti Polar Lipids Inc.	845875
LPE 18:1	Avanti Polar Lipids Inc.	846725
PA 16:0/18:1	Avanti Polar Lipids Inc.	840857
PS 16:0/18:1	Avanti Polar Lipids Inc.	840034
SM 18:1;O2/18:1	Avanti Polar Lipids Inc.	860587
Deuterated Acylcarnitine Mix	EURISO-TOP GmbH	NSK-B-1
FA 18:1	Sigma Aldrich	O1008
FA 18:0 ([13]C1) (99 atom% 13C)	Sigma Aldrich	299162
FC	Sigma Aldrich	C8667
CE18:0	Sigma Aldrich	C79409
MAG Mix – 1	Larodan Inc.	90-3001
DG 18:1/18:1/0:0 ([13]C3)	Larodan Inc.	78-1892-7
DG 16:0/16:0/0:0	Sigma Aldrich	D9135
TAG Mix – 10	Larodan Inc.	90-3010
TG 18:1/18:1/18:1 ([13]C3)	Larodan Inc.	78-1891-7
TG 16:0/16:0/16:0 ([13]C3)	Larodan Inc.	79-1600-7
TG Standard Mix – GLC 768	Nu-Chek Prep Inc.	GLC-768
TG Standard Mix 2 – GLC 406	Nu-Chek Prep Inc.	GLC-406
TG 20:1/20:1/20:1	Nu-Chek Prep Inc.	T-270
TG 20:2/20:2/20:2	Nu-Chek Prep Inc.	T-280
TG 20:3/20:3/20:3	Nu-Chek Prep Inc.	T-290
TG 20:4/20:4/20:4	Nu-Chek Prep Inc.	T-295
TG 20:5/20:5/20:5	Nu-Chek Prep Inc.	T-325
TG 14:1/14:1/14:1	Nu-Chek Prep Inc.	T-205
TG 16:1/16:1/16:1	Nu-Chek Prep Inc.	T-215
TG 16:0/16:0/18:1	Larodan Inc.	34-1602
Liquid and thin-layer chromatography equipment		
HybridSPE® – Phospholipid, 30 mg/1 ml	Merck KGaA	55261-U
Strata® NH2, 55 μm, 70 Å, 200 mg/3 ml	Phenomenex Inc.	8B-S009-FBJ
Accucore C30 column (150 × 2.1 mm; 2.6 μm, 150 Å)	Thermo Fisher Scientific	27826-152130
Accucore C18 column (150 × 2.1 mm; 2.6 μm, 150 Å)	Thermo Fisher Scientific	16126-152130

(*Continued on next page*)

Continued

REAGENT or RESOURCE	SOURCE	IDENTIFIER
Acquity UPLC BEH HILIC Si column (100 × 1.0 mm; 1.7 μm, 130 Å)	Waters Corp.	186003458
HPTLC silica gel plates 60, 20x10 cm	Merck KGaA	1.05633.0001
Solvents and additives		
Acetonitrile (ULC/MS-CC/SFC grade)	Biosolve	0001204102BS
2-Propanol (*i*-PrOH) (ULC/MS-CC/SFC grade)	Biosolve	0016264102BS
Methanol (ULC/MS-CC/SFC grade)	Biosolve	0013684102BS
Formic acid (ULC/MS-CC/SFC grade)	Biosolve	00069141A8BS
Chloroform (Emsure®)	Sigma Aldrich	1024451000
Methyl-tert-butyl-ether (≥99%)	Sigma Aldrich	34875
Ammonium formate (MS grade)	Sigma Aldrich	70221
Ammonium acetate (MS grade)	Sigma Aldrich	73594
Ethanol (Rotisolv®)	Carl Roth GmbH+Co. KG	P076.1
Acetone (≥99.9%)	Carl Roth GmbH+Co. KG	KK40.1
n-hexane (Rotisolv®, HPLC)	Carl Roth GmbH+Co. KG	7339.2
Acetic acid (100%, p.a.)	Carl Roth GmbH+Co. KG	3738.2
Software and algorithms		
LipidHunter	[21]	https://github.com/SysMedOs/lipidhunter
LipoStar	[22]	https://moldiscovery.com/software/lipostar/
LipidSearch™	Thermo Fisher Inc.	IQLAAEGABSFAPCMBFK
Merging identification lists from various software tools	This paper	https://github.com/SysMedOs/AdipoAtlasScripts
OriginPro 2017	OriginLab Corp.	https://www.originlab.com/index.aspx?go=Products/Origin/2017&pid=3240
Graphpad Prism Version 5.02	GraphPad Software	https://graphpad.com
Metaboanalyst	[60]	https://www.metaboanalyst.ca/
Deposited data		
Raw and analyzed data	Raw data	https://massive.ucsd.edu/ProteoSAFe/static/massive.jsp (MSV000086729); https://metabolomicsworkbench.org (http://www.metabolomicsworkbench.org/data/DRCCMetadata.php?Mode=Project&ProjectID=PR001112)
Biological samples		
Visceral and subcutaneous white adipose tissue biopsies of lean and obese patients	Leipzig Obesity BioBank	N/A

RESOURCE AVAILABILITY

Lead contact

Further information and requests for resources and reagents should be directed to and will be fulfilled by the Lead Contact, Maria Fedorova (maria.fedorova@tu-dresden.de)

Materials availability

This study did not generate new unique reagents

Data and code availability

All raw lipidomics data have been deposited at https://massive.ucsd.edu/ProteoSAFe/static/massive.jsp and https://metabolomicsworkbench.org are publicly available as of the date of publication. Accession numbers and DOI are listed in the Key resources table.

All original code has been deposited at GitHub repository and is publicly available as of the date of publication. Accession links are listed in the Key resources table.

Any additional information required to reanalyze the data reported in this work paper is available from the Lead Contact upon request.

EXPERIMENTAL MODEL AND SUBJECT DETAILS

Samples of human white adipose tissue from a total of 86 donors were kindly provided by Matthias Blüher as a part of Leipzig Obesity BioBank. Tissue collection was approved by the Ethics committee of the University of Leipzig (approval number: 159-12-21052012) and all subjects gave written informed consent before taking part in the study. Removed tissue samples were flash frozen in liquid nitrogen and stored at −80°C until further analysis. For the purpose of this study, we included adipose tissue samples from abdominal visceral (VAT) and subcutaneous (SAT) fat depots of lean (n = 5; BMI = 23.1 ± 1.5 kg/m^2; age = 68 ± 10.9 y; male/female = 3/2) and obese (n = 81; BMI = 45.1 ± 1.2 kg/m^2; age = 45 ± 2.2 y; male/female = 26/55) individuals from Caucasian population. Representative tissue pools were generated according to depot and phenotype specificity (Figure 1A).

METHOD DETAILS

Sample preparation

75 mg (for workflow optimization) or 50 mg (for LC-MS analysis) of frozen adipose tissue (AT) were cut on ice and collected into Lysing Matrix tubes containing ceramic beads (lysing matrix D, (1/8"), 2 ml, MP Biomedicals, Eschwege, Germany). All the applied solvents were supplemented with 0.1% (w/v) BHT and extraction was performed on ice. Extraction ratio AT [mg] / Extraction solvent [mL] was 10. For LC-MS analysis in-house designed WAT Lipid Standards Mixture (100 μL, in $CHCl_3$/MeOH (2:1, v/v); Table S2) was spiked before homogenization.

Lipid extraction

Folch method

AT was homogenized in 1 mL of MeOH by FastPrep24™ 5G (3x30s, Lysing Matrix D) with cooling on ice after each homogenization round. Homogenate were transferred into glass tubes (11.5 mL, round bottom culture tubes, VWR) using glass Pasteur pipettes. Beads and lysing tubes were washed with MeOH (400 μL) and $CHCl_3$ (1000 μL), solution was transfer into glass tube. $CHCl_3$ (1.8 mL) was added (to reconstitute ratio $CHCl_3$/MeOH = 2:1, v/v). Mixture was incubated on the roller mixer (4°C, 1 h, 210 rpm), and H_2O (840 μL) was added (to reconstitute ratio $CHCl_3$/MeOH/H_2O = 8:4:3, v/v), incubated on roller mixer (4°C, 10 min, 210 rpm), and centrifuged to achieve phase separation (4°C, 10 min, 2000 x g). ThelLower phase was collected. Extracts were dried *in vacuo* (Eppendorf concentrator 5301, 1 mbar).

Methyl tert-butyl ether (MTBE) method

AT was homogenized in 1 mL of MeOH by FastPrep24™ 5G (3x30s, Lysing Matrix D mode) with cooling on ice after each homogenization round. Homogenate were transferred into glass tubes (11.5 mL, round bottom culture tubes, VWR) using glass Pasteur pipettes. Beads and lysing tubes were washed with MTBE (1000 μL), and the solution was transferred to a glass tube. MTBE (3.95 mL) and MeOH (500 μL) were added (to reconstitute ratio MTBE/MeOH = 3.3:1, v/v). Mixture was incubated on roller mixer (4°C, 1 h, 210 rpm), and H_2O (1240 μL) was added (to reconstitute ratio MTBE/MeOH/H_2O = 3.3:1:0.8, v/v), incubated on roller mixer (4°C, 10 min, 210 rpm), and centrifuged to achieve phase separation (4°C, 10 min, 2000 × g). Upper organic phase with collected with Pasteur pipette. Re-extraction was done by adding MTBE/MeOH/H_2O (1.95 mL; 10:3.3:2.5, v/v) with subsequent incubation on the roller mixer (4°C, 10 min, 210 rpm) and centrifugation (4°C, 10 min, 2000 × g) to achieve phase separation. Organic phases were combined and dried *in vacuo* (Eppendorf concentrator 5301, 1 mbar).

Hexane/i-PrOH/HOAc method

AT was homogenized in 1 mL of MeOH by FastPrep24™ 5G (3x30s, Lysing Matrix D mode) with cooling on ice after each homogenization round. Homogenate were transferred into glass tubes (11.5 mL, round bottom culture tubes, VWR) using glass Pasteur pipettes. Beads and lysing tubes were washed with hexane (Hex; 1000 μL), solution was transfer to glass tube. Hex (350 μL), i-PrOH (350 μL), HOAc (105 μL; 100%, Roth), and H_2O (1.125 mL) were added to glass tube (to reconstitute ratio HOAc/i-PrOH/Hex = 2:20:30, v/v; Mix/H_2O = 2.5:1, v/v). Mixture was incubated on a roller mixer (4°C, 1 h, 210 rpm), Hex (3.75 mL) was added, incubate on the roller mixer (4°C, 10 min, 210 rpm), and centrifuged to achieve phase separation (4°C, 10 min, 2000 x g). Upper organic phase was collected with Pasteur pipette. Re-extraction was done by adding Hex (3.75 mL) with subsequent incubation on the roller mixer (4°C, 10 min, 210 rpm), and centrifugation (4°C, 10 min, 2000 x g) to achieve phase separation. Organic phases were combined and dried *in vacuo* (Eppendorf concentrator 5301, 1 mbar).

Protein concentration determination

Aqueous phases after lipid extraction were dried *in vacuo* (Eppendorf concentrator 5301, 1 mbar), redissolved in the buffer containing 7 M urea, 2 M thiourea, 1% sodium deoxycholate, 50 mM Tris-HCl, pH 7.5 and protein concentration was determined by Bradford assay.[61]

Lipid fractionation

Liquid-liquid extraction (LLE)[62]

AT lipid extract corresponding to 20 (for workflow optimization) or 45 mg (for LC-MS analysis) of AT was dried in a glass tube (11.5 mL, round bottom culture tubes, VWR). Hex (4.5 mL) and EtOH/H_2O (1.5 mL, 87:13, v/v) were added, tubes were vigorously vortexed (Tube A). Separated EtOH/H_2O phase was transferred into second glass tube containing 4.5 mL Hex (Tube B), vigorously vortexed, and the resulting EtOH/H_2O phase was transferred into an empty glass tube (Tube C). New portion of EtOH/H_2O (1.5 mL, 87:13, v/v) was added to the remaining Hex phase in Tube A, vortexed and transferred to Tube B, vortexed again and transferred to Tube C. This procedure was repeated six more times (in total eight times of EtOH/H_2O extraction from the original Hexane fraction). All collected EtOH/H_2O phases were combined and dried *in vacuo* (Eppendorf concentrator 5301, 1 mbar).

Zr-SPE[63]

Dry AT lipid extract corresponding to 20 mg of AT dissolved in $CHCl_3$/MeOH (150 μL; 2:1, v/v). Formic acid (0.1% v/v) acidified MeCN (900 μL) was added. Solution was loaded onto dry SPE cartridge (HybridSPE® – Phospholipid, 30 mg/1 ml, Lot: 4800102, Supelco), washed subsequently with formic acid (0.1% v/v) acidified MeCN (1 mL), MeCN (1 mL), and eluted with MeCN containing 5% (w/v) NH_4OH (2 × 1 mL). Eluates were dried *in vacuo* (Eppendorf concentrator 5301, 1 mbar).

LipFracSPE (based on[64] *with modifications)*

Dry AT lipid extract corresponding to 20 mg of AT dissolved in $CHCl_3$/MeOH (300 μL; 2:1, v/v). SPE cartridge (Strata® NH_2, 55 μm, 70 Å, 200 mg/3 ml, Lot: S17-003383, Phenomenex) was conditioned with Hexane (6 mL), and equilibrated with $CHCl_3$ (6 mL). AT lipids were loaded, and eluted subsequently with $CHCl_3$/i-PrOH (2:1, v/v, 15 mL, *unpolar fraction*), Et_2O/HOAc (100:2, v/v, 5 mL, *fatty acids fraction*), MeOH (5 mL, *neutral phospholipids fraction*) and Hex/i-PrOH/EtOH/0.1 M NH_4OAc (420:350:100:50, v/v + 5% HOAc (v/v), 5 mL, *acidic phospholipids fraction*). Acidic phospholipids fraction was neutralized by adding NH_4OH (25%; w/v; 0.75 mL), followed by the addition of H_2O (0.3 mL) and $CHCl_3$ (1 mL). Mixture was centrifuge (3 min, RT, 2000 × g) to induce phase separation, and lower organic phase was collected. Re-extraction was done by adding $CHCl_3$ (2 × 1 mL) with subsequent centrifugation (3 min, RT, 2000 × g). Organic phases were combined and dried *in vacuo* (Eppendorf concentrator 5301, 1 mbar).

Phospholipid quantification by ^{31}*P-NMR spectroscopy*[65]

Dried lipid extracts were resuspended in buffer containing 200 mM sodium cholate, 5 mM EDTA, 50 mM Tris-HCl, pH 7.65 (500 μL) by vigorous vortexing for 2 min. Samples were placed in 5 mm NMR tubes and ^{31}P-NMR spectra were recorded on a Bruker DRX-600 spectrometer operating at 242.88 MHz. All measurements were performed using a selective ^{31}P/^{1}H NMR probe at 37°C with composite pulse decoupling (Waltz-16) to eliminate ^{31}P–^{1}H coupling. Pulse intervals of the order of T_1 were used to allow quantitative analysis of phospholipid integral intensities. Other NMR parameters were as follows: acquisition time 1 s, data size 8–16 k, 60° pulse, pulse delay 2 s and a line-broadening (LB) of 1 Hz. Chemical shifts were referenced to the resonance of di-lauroyl-phosphatidic acid that was added as concentration and frequency standard. Further details are available in.[66]

Quantitative high performance thin layer chromatography (qHPTLC)

Unpolar lipids

AT lipid extracts were dissolved in $CHCl_3$/MeOH (2:1, v/v), and an amount corresponding to 1-10 μg AT wet weight were loaded using Camag Linomat 5 (Camag, Switzerland) on TLC plates (HPTLC silica gel 60, 20x10 cm, Merck). On each plate 7 dilutions of unpolar lipid TLC standards were loaded for quantitative lipid class specific calibration (Table 1). Plates were developed using hexane/Et_2O/HOAc (8:2:1, v/v). Dried TLC plates were immersed in acetone/H_2O (8:2, v/v) containing primuline (0.05%, w/v) for 5 s (Camag Chromatogramm Immersion Device III). Images were acquired with a CCD camera (Bio-Rad ChemiDoc MP, Bio-Rad) using the primuline fluorescence (Ex: Blue Epi light illumination; Em: Filter 530/28). Densitometric analysis was performed with Image Lab (Version 5.2.1, Bio-Rad).

Polar lipids

AT lipid extract polar fractions were dissolved in $CHCl_3$/MeOH (2:1, v/v), and amount corresponding to 1-5 mg AT wet weight were loaded using Camag Linomat 5 (Camag, Switzerland) on TLC plates (HPTLC silica gel 60, 20x10 cm, Merck). On each plate 7 dilutions of polar lipid TLC standards were loaded for quantitative lipid class specific calibration (Table 1). Plates were developed using $CHCl_3$/EtOH/TEA/H_2O (5:5:5:1, v/v). Dried TLC plates were immersed in acetone/H_2O (8:2, v/v) containing primuline (0.05%, w/v) for 5 s (Camag Chromatogramm Immersion Device III). Images were acquired with a CCD camera (Bio-Rad ChemiDoc MP, Bio-Rad) using the primuline fluorescence (Ex: Blue Epi light illumination; Em: Filter 530/28). Densitometric analysis was performed with Image Lab (Version 5.2.1, Bio-Rad).

Liquid-extraction static acquisition mass spectrometry

TLC plates were analyzed by using a TLC spot extraction system (Plate Express, Advion) coupled online to electrospray (ESI) Ion-Trap (IT) MS (amaZon SL, Bruker). TLC spots were extracted using pure MeOH as extraction solvent. ESI-IT parameter were as follows: electrospray voltage: 5.5 kV, end plate offset: 500 V; nebulizer gas: 7 psi; dry gas: 3 L/min; capillary temperature: 240°C; sheath gas (He) flow rate: 25 arbitrary units. Spectra were acquired in enhanced resolution mode and recorded in either positive or negative polarity. A maximum ionization time of 50 ms was applied. Data were subsequently analyzed using *DataAnalysis* (Bruker Daltonics, Bremen, Germany)

Table 1. Unpolar lipid TLC standards used for qHPTLC lipid-class-specific quantification

Unpolar lipid TLC-ISTD							
Lipid	Calibration range [nmol]						
TG 16:0/16:0/18:1	36.00	18.00	7.20	3.60	1.80	0.36	0.18
FC	77.59	38.79	15.52	7.76	3.88	0.78	0.39
DG 16:0/16:0/0	52.73	26.37	10.55	5.27	2.64	0.53	0.26
CE 18:0	45.79	22.90	9.16	4.58	2.29	0.46	0.23
FA 18:1	106.21	53.10	21.24	10.62	5.31	1.06	0.53
Polar lipid TLC - ISTD							
Lipid	Calibration range [nmol]						
TG 16:0/16:0/18:1	36.00	18.00	7.20	3.60	1.80	0.36	0.18
PC 16:0/18:1	39.47	19.73	7.89	3.95	1.97	0.39	0.20
PA 16:0/18:1	43.05	21.52	8.61	4.30	2.15	0.43	0.22
FA 18:1	106.21	53.10	21.24	10.62	5.31	1.06	0.53
LPC 18:1	57.51	28.75	11.50	5.75	2.88	0.58	0.29
LPE 18:1	62.55	31.28	12.51	6.26	3.13	0.63	0.31
PE 16:0/18:1	41.78	20.89	8.36	4.18	2.09	0.42	0.21
PS 16:0/18:1	37.98	18.99	7.60	3.80	1.90	0.38	0.19
SM 18:1;O2/18:1	41.15	20.57	8.23	4.11	2.06	0.41	0.21

Chromatography

Unpolar lipid separation (C30 RPC)

Total lipid extracts (represented mostly by triacylglycerols) were reconstituted in $CHCl_3$/MeOH (2:1, v/v), required amount was transferred into HPLC vials and dried *in vacuo*. The dried lipids were reconstituted in i-PrOH/$CHCl_3$ (1:1, v/v) to a concentration of 2.5 $\mu g_{tissue}/\mu l_{i\text{-}PrOH}$ and 5 µl (= 12.5 μg_{tissue}) were loaded onto the column. Triacylglycerols were separated by reversed phase liquid chromatography (RPLC) on a Thermo Scientific Vanquish Horizon UHPLC system (Thermo Fisher Scientific, Germering, Germany) equipped with an Thermo Scientific Accucore C30 column (150 × 2.1 mm; 2.6 µm, 150 Å, Thermo Fisher Scientific, Sunnyvale, USA). Lipids were separated by gradient elution with solvent A (MeCN/H_2O, 1:1, v/v) and B (i-PrOH/MeCN/H_2O, 85:10:5, v/v) both containing 5 mM NH_4HCO_2 and 0.1% (v/v) formic acid. Separation was performed at 50°C with a flow rate of 0.3 mL/min using the following gradient: 0-5 min – 50 to 80% B (curve 5), 5-22 min – 80 to 95% B (curve 4), 22-26 min – 95% isocratic, 26-27 min – 95 to 100% B (curve 5), 27-47 min – 100% B isocratic, 47-47.1 min – 100 to 50% B followed by 8 min re-equilibration at 50% B.

Polar lipid separation (C18 RPC)

Polar lipid fraction was reconstituted in $CHCl_3$/MeOH (2:1, v/v), required amount was transferred into HPLC vials and dried *in vacuo*. The dried lipids were reconstituted in pure i-PrOH to a concentration of 0.5 $mg_{tissue}/\mu l_{i\text{-}PrOH}$ and 5 µl (= 2.5 mg_{tissue}) were loaded onto the column. Polar lipid fractions (lyso-/phospholipids, sphingolipids, diacylglycerols) were separated by reversed phase liquid chromatography (RPLC) on a Vanquish Horizon UHPLC system (Thermo Fisher Scientific, Germering, Germany) equipped with an Thermo Scientific Accucore C18 column (150 × 2.1 mm; 2.6 µm, 150 Å, Thermo Fisher Scientific, Sunnyvale, USA). Lipids were separated by gradient elution with solvent A (MeCN/H_2O, 1:1, v/v) and B (i-PrOH/MeCN/H_2O, 85:10:5, v/v/v) both containing 5 mM NH_4HCO_2 and 0.1% (v/v) formic acid. Separation was performed at 50°C with a flow rate of 0.3 mL/min using following gradient: 0-20 min – 10 to 86% B (curve 4), 20-22 min – 86 to 95% B (curve 5), 22-26 min – 95% isocratic, 26-26.1 min – 95 to 10% B (curve 5) followed by 5 min re-equilibration at 10% B.

Acylcarnitine separation (Si HILIC)

Polar lipid fraction was reconstituted in $CHCl_3$/MeOH (2:1, v/v), required amount was transferred into HPLC vials and dried *in vacuo*. The dried lipids were reconstituted in pure i-PrOH to a concentration of 0.5 $mg_{tissue}/\mu l_{i\text{-}PrOH}$ and 5 µl (= 2.5 mg_{tissue}) were loaded onto the column. Acylcarnitines were separated by hydrophilic interaction chromatography (HILIC) on a Vanquish Horizon UHPLC system (Thermo Fisher Scientific) equipped with an Acquity UPLC BEH HILIC Si column (100 × 1.0 mm; 1.7 µm, 130 Å, Waters Corp.). Lipids were separated as described previously[67] by gradient elution with solvent A (MeCN/H_2O, 96:4, v/v) and B (H_2O) both containing 7 mM NH_4OAc. Separation was performed at 40°C with a flow rate of 0.15 ml/min using following gradient: 0-10 min – 0 to 10% B (curve 5), 10-10.1 min – 10 to 0% B (curve 5) followed by 5 min re-equilibration at 0% B.

Mass spectrometry

Each sample was analyzed on different LC-MS platforms. High resolution accurate mass (HRAM) orbitrap based MS was employed in combination with C18 and C30 RPC, or HILIC chromatographic separation. Overall, 111 LC-MS/MS analysis were performed for WAT lipids identification.

Data dependent acquisition on Q Exactive Plus Hybrid Quadrupole Orbitrap mass spectrometer

C18, C30 RPC and HILIC were coupled on-line to Thermo Scientific Q Exactive Plus Hybrid Quadrupole Orbitrap mass spectrometer (Thermo Fisher Scientific, Bremen, Germany) equipped with a HESI probe. Mass spectra were acquired in positive and negative modes with the following ESI parameters: sheath gas – 40 a.u., auxiliary gas – 10 L/min, sweep gas – 1 L/min, spray voltage – 3.5 kV (positive ion mode); −2.5 kV (negative ion mode), ion transfer temperature - 300°C, S-lens RF level – 35% and aux gas heater temperature – 370°C. For polar, unpolar lipids and acylcarnitines identification data were acquired in data dependent acquisition (DDA) modes with survey scan resolution of 140 000 (at *m/z* 200), AGC target 1e6 Maximum IT 100 ms in a scan range of *m/z* 350-1200 (380-1200 for unpolar lipids, 150-1200 for acyl carnitines). Data dependent MS2 were acquired with a resolution settings of 17 500 at 200 *m/z*, AGC target 1e5 counts, Maximum IT 60 ms, loop count 15, isolation window 1.2 *m/z* and stepped normalized collision energies of 10, 20 and 30% (15, 20 and 30% for unpolar lipids). A data dependent MS2 was triggered when an AGC target of 2e2 (2e3 for unpolar lipids, 2e1 for acyl carnitines) was reached followed by a Dynamic Exclusion for 10 s. All isotopes and charge states > 1 were excluded. All data was acquired in profile mode.

Data dependent acquisition on Orbitrap Fusion Lumos Tribrid mass spectrometer

C30 RPC were coupled on-line to Thermo Scientific Orbitrap Fusion Lumos Tribrid mass spectrometer (Thermo Fisher Scientific, San Jose, USA) equipped with a HESI probe. Mass spectra were acquired in positive and negative modes with the following ESI parameters: sheath gas – 40 L/min, auxiliary gas – 10 L/min, spray voltage – +3.5 kV and −2.8 kV, capillary temperature – 250°C, S-lens RF level – 25 and aux gas heater temperature – 320°C. Data was acquired in data dependent acquisition mode with survey scan resolution of 120 000 (at *m/z* 200), AGC target 4e5, Maximum IT 100 ms in a scan range of *m/z* 500-950. Data dependent MS2 spectra were acquired with the following settings: automatic gain control target: 4e5 counts; max. injection time: 100 ms. The filters used were MIPS (small molecule), precursor selection range (500-950), charge state (1), dynamic exclusion (exclusion duration 8 s, exclude isotopes, mass tolerance ± 5 ppm) and target exclusion (polarity specific). MS/MS spectra were acquired in the Ion Trap mass analyzer at rapid scan rate (HCD, stepped collision energy: 10, 20, 30%; Isolation Window: 1.2 *m/z*; automatic gain control target: 2e4 counts; max. injection time: 35 ms, centroid data type).

Acquire X on Orbitrap Fusion Lumos Tribrid mass spectrometer for in-depth triacylglycerol identification

Deep scan AcquireX Intelligent Data Acquisition Technology method was used to ensure in-depth identification of AT triacylglycerols. Two instrument methods were used – Full MS and ddMS[4]. The exclusion override factor was set to 10 and $[M+H]^+$, $[M+NH_4]^+$, $[M+Na]^+$ were selected as preferred ions. Three solvents blank replicate were analyzed before sample injection and the latest was used as exclusion reference. Injection volume was always 1 μL. A Orbitrap Fusion Lumos Tribrid Mass Spectrometer (Thermo Fisher Scientific, San Jose, USA) using a HESI source was operated in positive ion mode using the following parameters: spray voltage – +3.5 kV, ion transfer tube temperature – 250°C, sheath gas – 30 arbitrary units, aux gas – 10, sweep gas – 1, arbitrary units, vaporizer temperature – 300°C. Full MS were performed by the Orbitrap mass analyzer, operated at a resolution setting of 120,000 for *m/z* 200, scan range of *m/z* 500–1200, AGC target 4e5 counts, maximum IT 100 ms, RF level: 25%, data type profile, EASY-IC internal calibration. For MS/MS resolution setting of 15,000 for *m/z* 200, HCD (collision energy: 20, 35, 50%), isolation window of 1.2 *m/z*, AGC target 2e4, Maximum IT 40 ms, data type centroid were used. The filters used were MIPS small molecule, precursor selection range (*m/z* 500-1200), charge state 1, dynamic exclusion for 6 s, exclude isotopes, mass tolerance ± 10 ppm, and Xcalibur Acquire X generated exclusion and inclusion lists (mass tolerance 25 ppm). The MS3 and relative MS4 spectra were acquired only for ions which fulfilled the two following filters: acquisition neutral loss ion trigger and loss trigger (list of FA, tolerance ± 20 ppm). MS3 spectra were acquired in the orbitrap mass spectrometer at resolution settings of 15000 for *m/z* 200 (HCD, Collision Energy: 35%; Isolation Window: 1; automatic gain control target: 2e4 counts; max. injection time: 25 ms, centroid). MS4 analysis were performed in the ion trap at normal scan rate (CID, Collision Energy: 30%; Activation time: 10 ms; Activation Q: 0.25, Isolation Window: 1; automatic gain control target: 2e4 counts; max. injection time: 35 ms, centroid).

Targeted identification of cholesteryl esters

The total lipid extract (unpolar fraction) was analyzed via C30 RPC coupled on-line to a Q Exactive Plus Hybrid Quadrupole Orbitrap mass spectrometer (Thermo Fisher Scientific, Bremen, Germany) equipped with a HESI probe. Mass spectra were acquired in positive mode with the following ESI parameters: sheath gas – 40 au, auxiliary gas – 10 au, sweep gas – 1 au, spray voltage – 3.5 kV, ion transfer temperature – 300°C, S-lens RF level – 35% and aux gas heater temperature – 370°C. For cholesteryl ester identification data were acquired in parallel reaction monitoring (PRM) mode. An inclusion list of the ammoniated adducts of 36 cholesteryl esters covering the range of fatty acids from 2 up to 22 carbons and 0 to 6 double bonds was employed. PRM data was acquired with a resolution setting of 17 500 at 200 *m/z*, AGC target 2e5 counts, Maximum IT 200 ms, isolation window 1.2 *m/z* and a normalized collision energy of 20% in profile mode.

Co-elution of short chain TGs, MGs, and acylcarnitine's with corresponding internal standards

The retention behavior of short chain TGs, MGs and acylcarnitines was additionally studied in C18 RPC for verification of their identification. The short chain TG mixture TAG-MIX-10 (Larodan, Solna, Sweden) was dissolved in $CHCl_3$/MeOH (2:1, v/v) and an amount corresponding to 2.5 μg total TG was transferred to an HPLC vial and dried *in vacuo*. Dried TAGs were redissolved in pure *i*-PrOH

(100 μL) and 5 μL were injected. TAGs were chromatographically separated by C18 RP and analyzed by MS in DDA mode as described above (Figure S2).

The MG mixture MAG-MIX-1 (Larodan, Solna, Sweden) was dissolved in $CHCl_3$/MeOH (2:1, v/v) and an amount corresponding to 1.5 μg total MG was transferred to an HPLC vial and dried *in vacuo*. Dried MGs were redissolved in pure *i*-PrOH (100 μL) and 5 μL were injected. MGs were chromatographically separated by C18 RP and analyzed by MS in DDA mode as described above (Figure S2).

The non-deuterated acylcarnitine mixture NSK-B-US-1 (Cambridge Isotope Laboratories, Inc., Tewksbury, Massachusetts, USA) was dissolved in 1 mL $CHCl_3$/MeOH (2:1, v/v) and 75 μL were transferred to an HPLC vial and dried *in vacuo*. Dried acylcarnitines were redissolved in pure *i*-PrOH (75 μL) and 5 μL were injected. Acylcarnitines were chromatographically separated by C18 RP or HILIC and analyzed by MS in DDA mode as described above (Figure S2).

Lipid identification

DDA and Acquire X LC-MS/MS datasets were used for lipid molecular species identification. Identification strategy relied on three independent software tools followed by manual annotation.

LipidSearch

Lipids were identified using Thermo Scientific LipidSearch software version 4.1 SP1 using the following key processing parameters: target database – general, precursor tolerance ± 5 ppm, product tolerance ± 20 ppm, product ion threshold 5%, m-score threshold 1, Quan *m/z* tolerance ± 5 ppm, Quan RT (retention time) range ± 0.5 min. According to the lipid class, the ion mode and the structure of the lipids the results where filtered according to the "Grades." (Lyso)phospholipids were identified with Grade A (diacyl forms) and Grade B (ether forms). Sphingomyelins were accepted at Grade C. Ceramides were used after filtering with Grade A and Grade C for corresponding water loss ions, and TG/DG lipids were identified with Grade A only.

LipidHunter[21]

LipidHunter 2 RC source code version was used (https://github.com/SysMedOs/lipidhunter) to identify phospholipids in negative mode ($[M+HCOO]^-$ for PC and $[M-H]^-$ all others) and glycerolipids ($[M+NH_4]^+$) in positive mode. Raw files were converted into mzML format using MSConvert from Proteowizard project (version 3.0.9134). Lipids were identified using the following parameters: mass accuracy at MS level - 5 ppm, MS intensity threshold - 3e3 counts, mass accuracy at MS/MS level - 20 ppm, MS/MS intensity threshold - 100 counts. Identifications were filtered for isotopic score $\geq$ 75, and rank score $\geq$ 30. The white list of considered fatty acyl chains included 123 fatty acids corresponding to the LipidSearch default configuration file "FattyAcidDefinition.xml" for inter-software compatibility. Weight Factors assigned to each FA neutral loss fragment ions were 40, 48 and 30% for PLs, DGs and TGs, respectively. The identification results were reviewed using interactive HTML report. The table output files from LipidHunter were filtered and merged. Additional filters applied for PLs identification included: isotope score $\geq$ 80, rank score $\geq$ 40, both FA residues identified (for O/P- containing PLs, only one FA residue should be present, rank score $\geq$ 30). For DGs and TGs, all FA residues have to be identified, the isotope score filter was set to $\geq$ 85.

Lipostar[22]

Lipostar (version 1.0.6, Molecular Discovery, Hertfordshire, UK) equipped with LIPID MAPS structure database (version December 2017) was used. The raw files were imported directly, and aligned using default settings. Automatic peak picking was performed with SDA smoothing level set to low and minimum S/N ratio 3. Automatic isotope clustering settings were set to 7 ppm with RT tolerance 0.2 min. An "MS2 only" filter was applied to keep only features with MS/MS spectra for identification. Following parameters were used for lipid identification: 5 ppm precursor ion mass tolerance and 10 ppm product ion mass tolerance. The automatic approval was performed to keep structures with quality of 3-4 stars. Identification results of each lipid class were exported separately into 3 files using the Lipostar export function: feature table, best 3 matches of each feature (with check chain fragments enabled), and all approved matches. Exported tables were used for additional filtering and generation of merged identification list. For all classes, a fragmentation score filter of 60 and at least 2 fragment matches were applied (for TG at least 3 fragment matches).

Merge of identification results

Results of software assisted lipid identification were merged, and only lipids fulfilling the following parameter were kept in the final list: lipid must be identified by at least two software, within $\Delta RT < 0.3$ min. A chain length filter according to the FA included 58 fatty acids (from C4 to C26; maximum of six double bonds) were applied to all software results. A set of customized python scripts was used to filter and merge the output files. The corresponding source code is available on GitHub (https://github.com/SysMedOs/AdipoAtlasScripts). Ether PLs identified by the software were manually corrected based of the retention time mapping.

Manual lipid annotation

Manual annotation and retention time mapping were performed as described at https://github.com/SysMedOs/AdipoAtlasScripts/blob/main/LipidIdentification/AdipoAtlas_Lipid_Identification_Manual.pdf.

Lipid quantification

LC-MS quantification of acylcarnitines, polar and unpolar lipids

For quantification purposes, the respective lipid classes were separated on a RPC C30, C18 or HILIC as described above. MS data were acquired in Full MS mode on a Q Exactive Plus Hybrid Quadrupol Orbitrap mass spectrometer in the positive and negative ion mode at the resolution of 140,000 at *m/z* 200, AGC target of 1e6 and a Maximum IT of 100 ms in the mass range from *m/z* 100 – 1500. Data were acquired in profile mode.

Generation of calibration curves of employed ISTD

In order to ensure linear response of the employed standards, internal calibration curves were generated for the respective ISTD. Varying concentrations of ISTD were spiked into ≈50 mg pooled WAT prior to lipid extraction to generate a 5-point internal calibration curve (Table 2). Lipids were extracted and ISTD derived signals were quantified. Additionally, isobaric or isomeric overlap with endogenous compounds during LC-MS analysis was excluded by close inspection of LC-MS derived data. Only calibration points resulted in a calibration curve with $R > 0.98$ were approved. Final ISTD concentration to spike for subsequent quantification had to display a relative standard deviation of < 20% and represent the linear response range. Final spiked concentrations are marked in bold in Table 2.

QUANTIFICATION AND STATISTICAL ANALYSIS

For quantification raw datasets of Full MS measurements were processed using Thermo Scientific TraceFinder 4.1 (Thermo Fisher Scientific, Bremen, Germany). Quantification was based on determination of area under curve (AUC) using following settings: mass tolerance – 5 ppm, area noise factor – 5, peak noise factor – 10, baseline window – 150, S/N ≥ 3 using ICIS detection algorithm. Signals to be quantified (adducts and in-source fragments) were determined based on measurement of representative lipid standards for each class as shown below (Table S3).

For quantification of cholesteryl esters, raw datasets were acquired in PRM mode as described above. Measurements were processed using TraceFinder™ 4.1 (Thermo Fisher Scientific, Bremen, Germany). Quantification was based on determination of area under curve (AUC) using following settings: mass tolerance – 20 ppm, area noise factor – 5, peak noise factor – 10, baseline window – 150, S/N ≥ 3 using ICIS detection algorithm.

Obtained AUC values for all adducts and in-source fragments of each lipid specie were summed up in order to display all-ion abundance of studied lipid species. AUC values were corrected for ^{13}C abundance (Type I correction following the guidelines of Lipidomics Standards Initiative[7] as described before:[68]

$$AUC_{n(k)total} = AUC_{n(k)}\left(1 + 0.0109n + \frac{0.0109^2 n(n-1)}{2}\right)$$

$AUC_{n(k)\ total}$ = total ion area under curve, $AUC_{n(k)}$ = quantified area under curve of monoisotopic mass, n = No. of C-Atoms, k = No. of double bonds

Due to incomplete labeling of ISTDs, AUC of deuterated ISTD for phospholipids, sphingomyelins and acyl carnitines were determined by summing up the AUC of $[M-2]^+$ (d_{x-2}), $[M-1]^+$ (d_{x-1}),$[M]^+$ (d_x), $[M+1]^+$ (d_x; $^{13}C_1$) and $[M+2]^+$ (d_x; $^{13}C_2$).

AUC of non-labeled ISTD for different ceramide classes were corrected for ^{13}C abundance (Type I correction following the guidelines of Lipidomics Standards Initiative[7] as described before:[68]

$$AUC_{n(k)total} = AUC_{n(k)}\left(1 + 0.0109n + \frac{0.0109^2 n(n-1)}{2}\right)$$

Quantitative values for lipid species were determined by relating AUC of the used ISTD to the lipid specie AUC:

$$C_{Lipid} = \frac{AUC_{Lipid}}{AUC_{ISTD}} * C_{ISTD}$$

C_{Lipid} = Concentration of lipid specie, C_{ISTD} = concentration of ISTD, AUC_{Lipid} = corrected area under curve for lipid specie, AUC_{ISTD} = area under curve for ISTD.

Response factors calculations for triacylglycerols

TGs were quantified using a single $^{13}C_3$ labeled TG molecular species (TG 18:1/18:1/18:1 ([13]C3)). Type II isotopic correction was applied for determination of AUC of $^{13}C_3$ labeled TG, due to coelution with the native TG and isobaric overlap of $[M]^+$ of $^{13}C_3$ labeled TAG and $[M+3]^+$ of native TG.

TG molecular species experience differential ionization and ion transmission yielding varying intensities depending on the molecular structure. Response factors of different native and isotopically labeled standards (Table S4) relative to the used $^{13}C_3$ labeled ISTD TG 18:1/18:1/18:1 ([13]C3) were determined in order to increase accuracy of TG quantification. Dilution series of 34 different labeled and unlabeled standards spanning over three orders of magnitude were recorded (Table S4). Calibration curves were generated for each species to yield linear regression models with a minimum $R^2 > 0.99$ and RSD < 10% for each point of the dilution curve. Obtained

Table 2. Spiked concentrations to generate an internal calibration curve

Lipid	Spiked in ≈ 50 mg WAT [nmol]					
SPLASH LIPIDOMIX						
PC 15:0_18:1 (d7)	0	0.107	0.213	1.067	2.134[a]	4.268
PE 15:0_18:1 (d7)	0	0.004	0.008	0.040	0.080[a]	0.160
PS 15:0_18:1 (d7)	0	0.003	0.005	0.027	0.054[a]	0.108
PG 15:0_18:1 (d7)	0	0.019	0.038	0.190	0.381[a]	0.762
PI 15:0_18:1 (d7)	0	0.005	0.011	0.054	0.107[a]	0.215
PA 15:0_18:1 (d7)	0	0.005	0.011	0.054	0.107[a]	0.215
LPC 18:1 (d7)	0	0.024	0.048	0.241	0.482[a]	0.965
LPE 18:1 (d7)	0	0.005	0.011	0.054	0.109[a]	0.218
CE 18:1 (d7)	0	0.271	0.541	2.705	5.411[a]	10.821
MG 18:1 (d7)	0	0.003	0.006	0.028	0.055[a]	0.110
DG 15:0_18:1 (d7)	0	0.008	0.016	0.080	0.160[a]	0.320
TG 15:0_18:1_15:0 (d7)	0	0.035	0.071	0.353	0.705[a]	1.411
SM d18:1_18:1 (d9)	0	0.021	0.042	0.209	0.419[a]	0.837
Chol (d7)	0	0.125	0.250	1.250	2.499[a]	4.999
Cer/SpH mix I (Avanti)						
SPB 17:1;O2	0	0.019	0.038	0.188	0.375[a]	0.750
SPB 17:0;O2	0	0.019	0.038	0.188	0.375[a]	0.750
SPBP 17:1;O2	0	0.019	0.038	0.188	0.375[a]	0.750
SPBP 17:0;O2	0	0.019	0.038	0.188	0.375[a]	0.750
Lac-Cer 18:1;O2/12:0	0	0.019	0.038	0.188	0.375[a]	0.750
Gluc-Cer d18:1;O2/12:0	0	0.019	0.038	0.188	0.375[a]	0.750
SM 18:1;O2/12:0	0	0.019	0.038	0.188	0.375[a]	0.750
Cer 18:1;O2/12:0	0	0.019	0.038	0.188	0.375[a]	0.750
CerP 18:1;O2/12:0	0	0.019	0.038	0.188	0.375[a]	0.750
Cer 18:1;O2/25:0	0	0.019	0.038	0.188	0.375[a]	0.750
Acylcarnitine NSK-1-B mix						
Free carnitine (d9)	0	0.008	0.016	0.081	0.162[a]	0.324
CAR 2:0 (d3)	0	0.002	0.004	0.018	0.037[a]	0.074
CAR 3:0 (d3)	0	0.000	0.001	0.004	0.007[a]	0.015
CAR 4:0 (d3)	0	0.000	0.001	0.004	0.007[a]	0.015
CAR 5:0 (d9)	0	0.000	0.001	0.004	0.007[a]	0.015
CAR 8:0 (d3)	0	0.000	0.001	0.004	0.007[a]	0.014
CAR 14:0 (d9)	0	0.000	0.001	0.004	0.007[a]	0.015
CAR 16:0 (d3)	0	0.001	0.002	0.008	0.015[a]	0.030
Additionally added						
FA 18:0 ([13]C1)	0	0.500	1.000	5.000	10.000[a]	20.000
TG 18:1/18:1/18:1 ([13]C3)	0	50.000	100.000	500.000	1000.000[a]	2000.000
TG 16:0/16:0/16:0 ([13]C3)	0	2.500	5.000	25.000	50.000[a]	100.000
DG 18:1/18:1/0:0 ([13]C3)	0	0.500	1.000	5.000	10.000[a]	20.000
Cer 18:0;O2/12:0	0	0.019	0.038	0.188	0.375[a]	0.750
Cer 18:0;O2/8:0	0	0.019	0.038	0.188	0.375[a]	0.750
Cer 18:1;O/6:0	0	0.019	0.038	0.188	0.375[a]	0.750
Cer 18:0;O3/16:0	0	0.019	0.038	0.188	0.375[a]	0.750
Cer 18:0;O3/8:0	0	0.019	0.038	0.188	0.375[a]	0.750
Cer 18:1;O2/17:0,O[2*R*-OH]	0	0.019	0.038	0.188	0.375[a]	0.750

[a]Final used ISTD concentration

slopes of concentration-response curves were related to the concentration-response curve of the isotopically labeled ISTD to establish response factors (RF). RF were normalized to the number of carbons and double bonds (DB) by dividing RF with the equivalent-carbon-number (ECN) yielding the normalized response factor (RF_{norm}). Deviations in response mainly arise from increasing unsaturation and therefore for each DB number RF_{norm} was separately related to *m/z* of $[M+NH_4]^+$. Resulting slopes and y-intercepts for each double bond number were used to establish a linear regression model for determination of slopes and y-intercepts for which no standard were available. Subsequently, RF_{norm} is calculated for each identified TG species and used for the quantification. A detailed description of the workflow provided in Figure S4. Finally, accurate quantification of TG was performed by relating the intensity of the ISTD and the RF-corrected intensity of the TG molecular species as expressed by the following equation:

$$AUC_{TG,corrected} = \frac{AUC_{TG}}{RF_{TG}}$$

$$C_{TG} = \frac{AUC_{TG,corrected}}{AUC_{ISTD}} * C_{ISTD}$$

Software

Tracefinder 4.1 (Thermo Fisher Scientific, Bremen, Germany) was used for targeted lipid quantification. Quantitative data analysis including isotopic correction, ISTD normalization and response factor normalization was performed with Microsoft Excel 2016. Graphical representations were generated with Graphpad Prism® 5.02 and OriginPro© 2017. Metaboanalyst (https://www.metaboanalyst.ca/) was used to generate heatmaps and perform statistical analysis. A lipid was found to be statistically significantly regulated by Students t test with a threshold of $p \leq 0.05$ (FDR adjusted) assuming equal variances and a fold change ≥ 2, or with an ANOVA $p \leq 0.05$.